Development of a Setup to test Time-Of-Flight Methods for the KATRIN Experiment

Bachelor Thesis

Richard W. J. Salomon

Themensteller: Prof. Dr. Christian Weinheimer
Zweitgutachter: Apl. Prof. Dr. Alfons Khoukaz
Westfälische-Wilhelms-Universität Münster
Institut für Kernphysik
AG Prof. Dr. C. Weinheimer

Plagiatserklärung der / des Studierenden

Hiermit versichere ich, dass die vorliegende Arbeit über „Development of a Setup to test Time-Of-Flight Methods for the KATRIN Experiment“ selbstständig verfasst worden ist, dass keine anderen Quellen und Hilfsmittel als die angegebenen benutzt worden sind und dass die Stellen der Arbeit, die anderen Werken – auch elektronischen Medien – dem Wortlaut oder Sinn nach entnommen wurden, auf jeden Fall unter Angabe der Quelle als Entlehnung kenntlich gemacht worden sind.

_____

Datum, Unterschrift

Ich erkläre mich mit einem Abgleich der Arbeit mit anderen Texten zwecks Auffindung von Übereinstimmungen sowie mit einer zu diesem Zweck vorzunehmenden Speicherung der Arbeit in eine Datenbank einverstanden.

_____

Datum, Unterschrift

Contents

1. Introduction

Ever since Pauli first postulated the existence of the neutrino many scientists have taken on the challenge to discover the fundamental properties of the neutrino. But as of yet it has not been possible to determine the mass of the neutrino. The Karlsruhe Tritium Neutrino (KATRIN) experiment aims at determining the electron antineutrino mass scale. The main idea of KATRIN is to precisely measure the endpoint region of the electron spectrum following a tritium β^- decay

$$ {}^{3}_{1}\mathrm{H} \rightarrow {}^{3}_{2}\mathrm{He}^{+} + \mathrm{e}^{-} + \bar{\nu_e}. \tag{1.1} $$

Upper limits of $2.05\,\mathrm{eV/c^2}$ [1] and $2.3\,\mathrm{eV/c^2}$ [2] (both 95 % C.L.) have already been set by predecessor experiments at Troitsk and Mainz using the same technique. KATRIN now aims to further improve this limit to $0.2\,\mathrm{eV/c^2}$ (90 % C.L.) or, if $m_\nu > 0.35\,\mathrm{eV/c^2}$ to find the neutrino mass with a discovery potential of 5σ [3]. A successful first scientific run of KATRIN over a duration of four weeks in spring 2019 improved the former results by a factor two. An upper limit of 1.1 eV at 90% confidence was derived [4].
This thesis focuses on the development of a setup that will be able to test numerous ideas to further improve KATRIN's sensitivity with the main focus on time-of-flight (TOF) methods.

1.1. The KATRIN Experiment

In the following section a brief overview of the KATRIN experiment will be given.
As written above, KATRIN tries to measure the endpoint $E_0 = 18.6\,\mathrm{keV}$ of a tritium β-decay (see eq. (1.1)). The energy released during this process is distributed statistically among the electron and the neutrino. The resulting energy spectrum of the electron is shown in fig. 1.1. Most relevant for the experiment is the case in which the kinetic energy of the electron reaches its maximum. As neutrino oscillation experiments safely indicate that the neutrino is indeed a massive particle [5], the endpoint energy of the electron spectrum will be reduced by the energy equivalent of the neutrino mass. This will also significantly change the shape of the spectrum in the endpoint region (as fig. 1.1 b) illustrates).
One can also deduce from the figure that only a tiny fraction of decays ($2{\cdot}10^{-13}$) falls into the last 1 eV below the endpoint [3]. This is why a tritium source with high luminosity is required. At KATRIN a windowless gaseous tritium source (WGTS) is installed at the beginning of the ~ 70 m long experimental setup (see fig. 1.2). Inside the 10 m long WGTS tube a decay rate of $9.5 \cdot 10^{10}$ β-decays per second can be achieved [6].
From there magnets adiabatically guide the electrons through the transport section

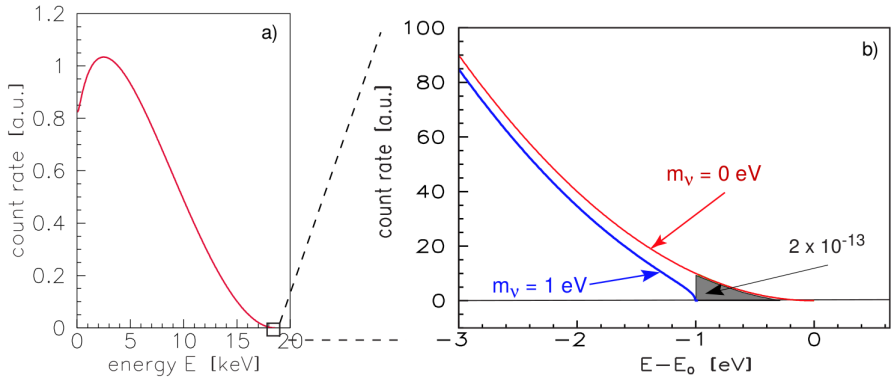

Figure 1.1.: Electron energy spectrum of a tritium β-decay. a) complete spectrum, b) magnification of the endpoint region of the spectrum ($m_\nu = 0\,\mathrm{eV/c^2}$ and $m_\nu = 1\,\mathrm{eV/c^2}$) [3]. One can see that the count rate at the endpoint region is close to 0. Only $2 \cdot 10^{-13}$ decays create an electron with a kinetic energy up to 1 eV below the endpoint.

where the remaining tritium flow is reduced by a factor of $\sim 10^{11}$ [3].
After having passed the transport section the electrons enter the pre-spectrometer where electrons that do not carry information about the neutrino mass (kinetic energy $E < 18.3$ keV) will be filtered out electrostatically by a retarding high voltage. The same principle but with a much better energy resolution is used in the main spectrometer. This type of spectrometer is called MAC-E filter (Magnetic Adiabatic Collimation with Electrostatic filter) and yields an integrated spectrum. A more in-depth explanation of the details of a MAC-E-filter can be found in section 2.1. The MAC-E filter used for the KATRIN experiment is able to achieve an energy resolution of $\Delta E = 0.93$ eV.
In the back of the setup a Si-PIN diode array counts all transmitted electrons.

1.2. TOF Methods at KATRIN

As the sensitivity of KATRIN is constrained by technical limits e.g. the diameter of the spectrometer and background processes, new methods are required to improve the sensitivity of the setup. A possible method to achieve such an improvement is to operate the MAC-E-filter in a time-of-flight mode [8] which means that the time it takes for an electron to pass the spectrometer is measured. While the standard MAC-E mode can only count the number of transmitted electrons one retarding potential at a time, TOF spectroscopy enables the measurement of a differential spectrum. This can be particularly useful because the TOF distribution does not only depend on the neutrino mass but also because small energy differences near the retarding potential lead to big differences in flight time. It has been shown that the statistical sensitivity of m_{ν_e} can be improved by a factor of more than 2 given a sufficient time resolution. However, there is

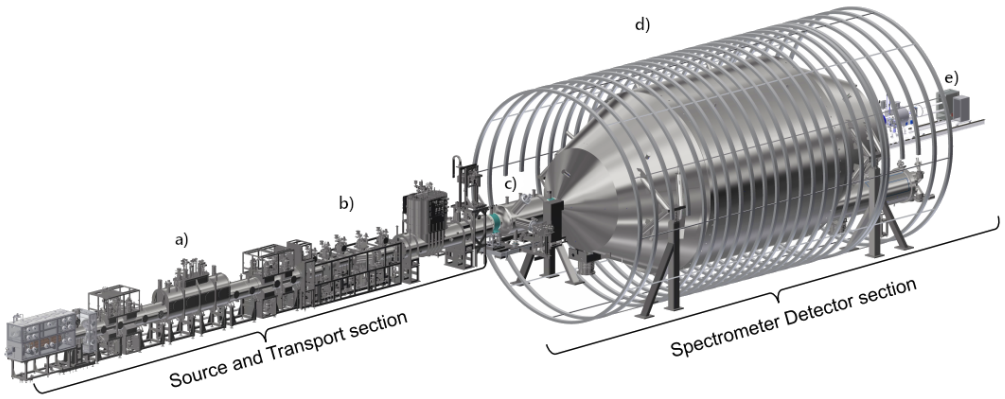

Figure 1.2.: Overview of the KATRIN experiment. (a) Windowless gaseous tritium source, (b) transport section, (c) pre-spectrometer, (d) main spectrometer, (e) detector system [7].

one major drawback associated with this method. For it to work, electrons need to be detected (tagged) as they enter the spectrometer. The challenge is to find a way that allows to extract a small but well-known amount of energy from the electrons. But as of yet, there exists no method to allow this kind of measurement.
Therefore, a different approach that avoids the usage of an electron tagger but still benefits from the gain of sensitivity by differential TOF measurements is being developed. The method of time-focusing time-of-flight (tfTOF) [9] aims to do just that. It plans to use a periodically varying electrostatic potential in such a way that electrons with a certain target energy arrive at the detector at the same time, regardless of their start time. This could in principal be implemented in the KATRIN main spectrometer. It could even be possible to simultaneously use the standard MAC-E filter mode together with the tfTOF mode.
The setup presented in this thesis is being built with these considerations in mind. It shall offer a good basis on which new methods, in particular TOF and tfTOF will be investigated.

2. MAC-E Filter and Time-Of-Flight Concepts

The MAC-E filter was first introduced in 1980 [10] and has been developed and adapted to suit the experiment's needs of high luminosity combined with sharp energy resolution. This chapter will cover the physical principles behind this technique and the transmission properties will be discussed. Moreover, the MAC-E filter can be used for (time-focusing) time-of-flight measurements. These techniques and the advantages for the KATRIN experiment will also be introduced.

2.1. MAC-E Filter

As already mentioned in section 1.1 KATRIN's spectrometers (pre-spectrometer and main spectrometer) are based on the principle of magnetic adiabatic collimation with electrostatic filtering. Mastering the basics of this technique is key to understanding the experiment as a whole.

2.1.1. Adiabatic Collimation

A general overview of the working principle of a MAC-E-filter is shown in fig. 2.1. This figure specifically shows the cross-section of the main spectrometer of the KATRIN experiment. Electrons inside the filter are guided magnetically from the spectrometer entrance to the detector. The guiding magnetic field is provided by two superconducting solenoids at the spectrometer entrance and the spectrometer exit. The motion of an electron with kinetic energy E and momentum $\vec{p}$ entering the spectrometer is therefore mainly influenced by the magnetic field $\vec{B}$. Due to the Lorentz force F_L the electron performs a cyclotron motion around a magnetic field line. The kinetic energy can then be separated into a component parallel ($E_\parallel$) and a component perpendicular ($E_\perp$) to the magnetic field:

$$E_\parallel = E \cdot \sin^2(\theta) \tag{2.1}$$

$$E_\perp = E \cdot \cos^2(\theta) \tag{2.2}$$

where $\theta = \theta\angle(\vec{B}, \vec{p})$ and $E = E_\parallel + E_\perp$. Thereby $E_\perp$ contributes to the cyclotron motion around the field line whereas $E_\parallel$ contributes to the motion in the direction of the field line [12].

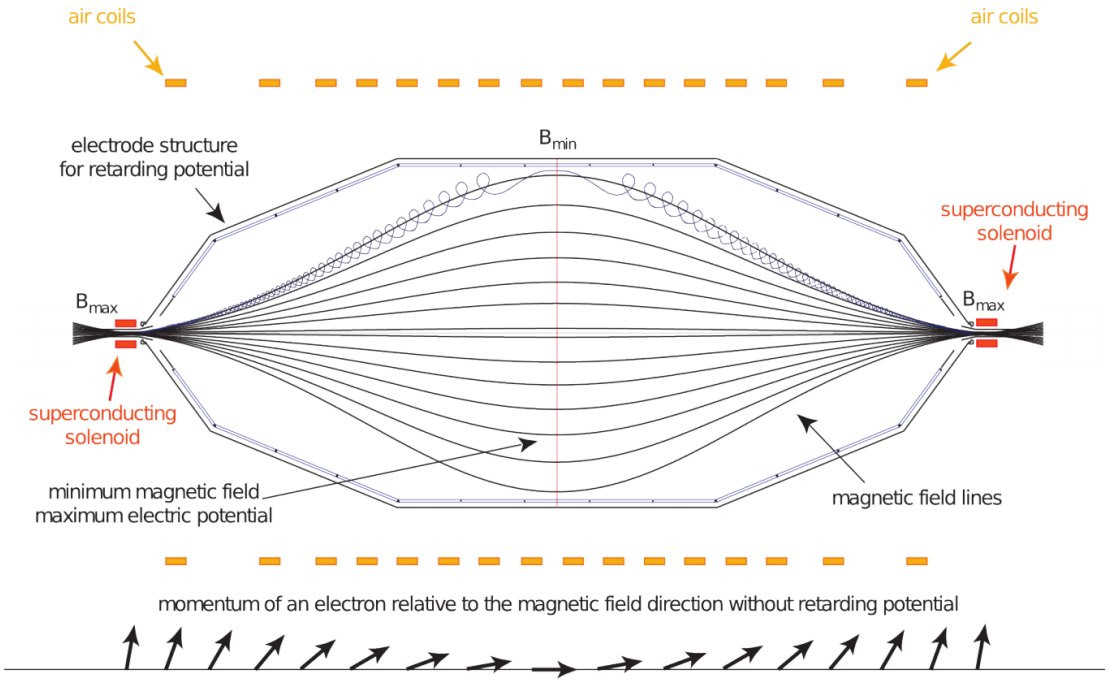

Figure 2.1.: Schematic drawing of the KATRIN main spectrometer. On both sides of the spectrometer superconducting coils are placed to create the magnetic field. The electrode structure is designed so that the retarding potential reaches its maximum when the magnetic field is minimal. For the uppermost magnetic field line an exaggerated cyclotron motion of an electron is shown. [11]

Considering the maximum value of the Lorentz factor with $E_{\mathrm{kin,\,max}} = 18.6\,\mathrm{keV}$

$$\gamma_{\mathrm{max}} = \frac{1}{\sqrt{1 - \frac{v^2}{c^2}}} = 1.04 \approx 1 \tag{2.3}$$

it is sufficient to use non-relativistic approximations for the following calculations.
An important concept for the MAC-E-filter is the concept of adiabatic invariance. For a gyrating electron with elementary charge e, mass m_e and orbital angular momentum $\vec{l}$ it can be shown that the magnetic momentum is conserved

$$\mu = \frac{e}{2m_e}\left|\vec{l}\right| = \frac{E_\perp}{\left|\vec{B}\right|} = \mathrm{const.} \tag{2.4}$$

if the change of the magnetic field over one cyclotron motion is small [13]. This means that the motion of an electron inside the MAC-E-filter is adiabatic if

$$\frac{1}{B}\frac{\mathrm{d}\vec{B}}{\mathrm{d}t} \ll \frac{\omega_c}{2\pi} \tag{2.5}$$

where $\omega_c = \frac{eB}{m_e}$ is the cyclotron frequency. Additionally, the total kinetic energy is conserved. Hence one can deduce that the transversal energy is transformed into longitudinal energy between the spectrometer entrance and the analyzing plane where the absolute value of the retarding potential is maximal. This is especially useful because the retarding potential only affects the longitudinal energy. Using the technique of adiabatic collimation therefore automatically increases the acceptance angle of the spectrometer to a theoretical value of 2π. The effect of adiabatic collimation is also illustrated in fig. 2.1. The arrows underneath the spectrometer drawing indicate the angle θ and thus the amount of transversal energy in comparison to the amount of longitudinal energy. Knowing the angle at a certain point i and using eq. (2.4) one can calculate the transversal energy at any point f in the spectrometer

$$E_{\perp,f} = E_{\perp,i} \cdot \frac{B_f}{B_i} \tag{2.6}$$

$$\Longrightarrow \sin^2(\theta_f) = \sin^2(\theta_i) \cdot \frac{B_f}{B_i}. \tag{2.7}$$

Furthermore the cyclotron radius $r_{\text{cycl.}}$ can be derived from the Lorentz force

$$F_L = e \cdot v_\perp B = m_e \cdot \frac{v_\perp^2}{r_{\text{cycl.}}} \tag{2.8}$$

$$\Longrightarrow r_{\text{cycl.}} = \frac{\sqrt{2m_e E_\perp}}{eB} \tag{2.9}$$

where $v_\perp$ denotes the transversal component of the electron's velocity.

2.1.2. Energy Resolution and Transmission Function

In this section the transmission properties as well as the energy resolution of a MAC-E filter will be discussed.
From eq. (2.6) one can see that it is realistically impossible to transform the whole transversal energy into longitudinal energy as the magnetic field would have to be infinitely small. Hence the energy resolution ΔE is finite. With eq. (2.6) the remaining transversal energy $E_{\perp,\text{ana}}$ at the analyzing plane of an electron with maximum transversal energy (start angle $\theta_{\text{start}} = 90°$) at the spectrometer entrance can be determined:

$$\Delta E_{\text{full}} = E_{\perp,\text{ana}} = E_{\perp,\text{start}} \cdot \frac{B_{\text{ana}}}{B_{\text{start}}} = E \cdot \frac{B_{\text{ana}}}{B_{\text{start}}}. \tag{2.10}$$

As stated above, a retarding high voltage (U_0) is used to filter out electrons below a certain energy threshold. As a consequence only electrons that satisfy

$$E_{\parallel,\text{ana}} - eU_0 > 0 \tag{2.11}$$

are able to pass the analyzing plane. Consequently, the MAC-E-filter serves as high pass filter which ultimately yields an integrated spectrum. Rewriting eq. (2.11) using that

the total kinetic energy is conserved yields

$$\begin{aligned} E_{\parallel,\mathrm{ana}} - eU_0 &= E_{\mathrm{start}} - E_{\perp,\mathrm{ana}} - eU_0 \\ &= E_{\mathrm{start}} - E_{\mathrm{start}} \cdot \sin^2(\theta_{\mathrm{start}}) \frac{B_{\mathrm{ana}}}{B_{\mathrm{start}}} - eU_0 > 0 \end{aligned} \tag{2.12}$$

This implies that there is a maximum transmission angle θ_{max}. Electrons that have a starting angle $\theta_{\mathrm{start}} > \theta_{\mathrm{max}}$ will not be transmitted. Solving eq. (2.12) for θ_{start} results in the following condition:

$$\theta_{\mathrm{start}} \leq \theta_{\mathrm{max}} = \arcsin \sqrt{\frac{E_{\mathrm{start}} - eU_0}{E_{\mathrm{start}}} \frac{B_{\mathrm{start}}}{B_{\mathrm{ana}}}}. \tag{2.13}$$

This expression can be used to determine the transmission function. The solid angle of a cone is defined by

$$\Delta\Omega = 2\pi(1 - \cos(\theta)). \tag{2.14}$$

In this case $\Delta\Omega(\theta_{\mathrm{max}})$ includes all transmitted electrons. The ratio of $\Delta\Omega(\theta_{\mathrm{max}})$ (using eq. (2.13)) to the theoretical acceptance angle of 2π gives the transmission probability

$$\frac{\Delta\Omega}{2\pi} = 1 - \cos(\theta_{\mathrm{max}}). \tag{2.15}$$

Using the relation $\cos(\arcsin(\sqrt{x})) = \sqrt{1-x}$ the transmission function of a MAC-E filter can be written as

$$T(E_{\mathrm{start}}, U_0) = \begin{cases} 0, & \text{for } E_{\mathrm{start}} < eU_0 \\ 1 - \sqrt{1 - \frac{E_{\mathrm{start}} - eU_0}{E_{\mathrm{start}}} \frac{B_{\mathrm{start}}}{B_{\mathrm{ana}}}}, & \text{for } eU_0 < E_{\mathrm{start}} < eU_0 + \Delta E_{\mathrm{full}} \\ 1, & \text{for } eU_0 + \Delta E_{\mathrm{full}} < E_{\mathrm{start}} \end{cases}. \tag{2.16}$$

This equation is valid as long as $B_{\mathrm{start}} = B_{\mathrm{max}}$ applies. However, at KATRIN electrons enter the spectrometer in a magnetic field $B_{\mathrm{start}} < B_{\mathrm{max}}$. This affects the transmission because the pitch angle θ increases proportionally to the magnetic field which entails that θ might rise above 90°. These electrons will then be reflected. This effect is well-known as the magnetic mirror effect.
Using eq. (2.6) with $E_{\mathrm{start}} = E_{\mathrm{max}} \geq E_{\perp,\mathrm{max}}$ one can calculate the maximum transmission angle

$$\theta_{\mathrm{start}} \leq \arcsin \sqrt{\frac{B_{\mathrm{start}}}{B_{\mathrm{max}}}}. \tag{2.17}$$

The transmission function must then take this effect into account. This is done by inserting the condition for the maximum starting angle from eq. (2.17) into eq. (2.15). The new transmission function then yields

$$T(E_{\mathrm{start}}, U_0) = \begin{cases} 0, & \text{for } E_{\mathrm{start}} < eU_0 \\ 1 - \sqrt{1 - \frac{E_{\mathrm{start}} - eU_0}{E_{\mathrm{start}}} \frac{B_{\mathrm{start}}}{B_{\mathrm{ana}}}}, & \text{for } eU_0 < E_{\mathrm{start}} < eU_0 + \Delta E \\ 1 - \sqrt{1 - \frac{B_{\mathrm{start}}}{B_{\mathrm{max}}}}, & \text{for } eU_0 + \Delta E < E_{\mathrm{start}} \end{cases} \tag{2.18}$$

with the new energy resolution $\Delta E = E_{\text{start}} \cdot \frac{B_{\text{ana}}}{B_{\text{max}}}$.
The magnetic configuration at KATRIN proposed in [3] is designed to achieve values of $B_{\text{max}} = 6\,\text{T}$, $B_{\text{start}} = 3.6\,\text{T}$ and $B_{\text{ana}} = 0.3\,\text{mT}$. This leads to the energy resolution of $\Delta E = 0.93\,\text{eV}$ and a maximum starting angle of $\theta_{\text{max, start}} \approx 50.77\,°$. The first measurement phase, however, reached an energy resolution of $\Delta E = 2.8\,\text{eV}$ with $B_{\text{max}} = 4.24\,\text{T}$ and $B_{\text{min}} = 0.63\,\text{mT}$ [4]. In theory, the new measurement setup, which is presented in

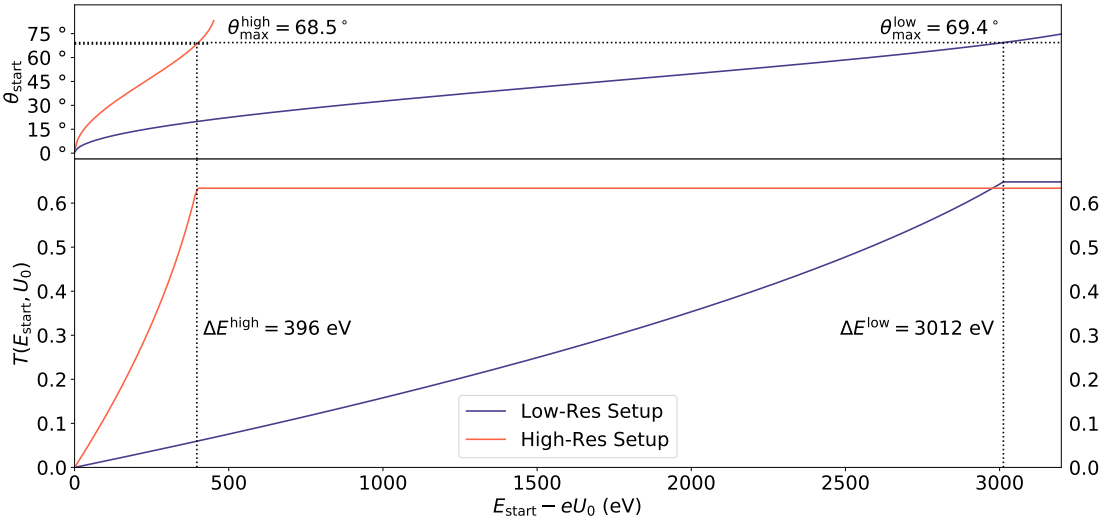

Figure 2.2.: Transmission functions of two different magnetic configurations of the new MAC-E filter setup. The red curve indicates a high resolution configuration with the energy resolution $\Delta E^{\text{high}} = 396\,\text{eV}$ ($B_{\text{max}} = 45.2\,\text{mT}$ and $B_{\text{ana}} = 1.4\,\text{mT}$). The blue curve shows a low resolution configuration with $\Delta E^{\text{low}} = 3012\,\text{eV}$ ($B_{\text{max}} = 53.6\,\text{mT}$ and $B_{\text{ana}} = 12.4\,\text{mT}$).
The bottom frame shows the transmission probability T according to eq. (2.18) for both configurations whereas the top frame shows the corresponding starting angle θ_{start} to a certain surplus energy $E_{\text{start}} - eU_0$ according to eq. (2.13).
The vertical lines indicate the respective energy resolution. These lines intersect with the functions in the top frame. These intersections are further marked by horizontal lines that visualize the maximum starting angle θ_{start}. Electrons that exceed this value at the start will be reflected magnetically.

detail in section 3.1, will reach an energy resolution of 396 eV. As this setup is designed to be very versatile in order to allow multiple different techniques to be tested, there are several parameters that can be configured. This means that the setup can be run with different transmission properties. It is also important to notice that the setup will be operated with a mono-energetic electron source that features an energy spread lower than 1 eV [12], thus reducing the importance of developing a high resolution spectrometer.

Figure 2.2 illustrates the transmission function of a high resolution scenario as well as a low resolution scenario. Additionally, the upper section of the figure shows the corresponding starting angle to a certain surplus energy (compare eq. (2.17)). Both scenarios are based on simulations using Kassiopeia (see section 4.2.3) and are mainly presented to give an example of what can be expected from the new setup.
The high-res scenario features magnetic field values of $B_{\mathrm{max}} = 45.2\,\mathrm{mT}$ and $B_{\mathrm{ana}} = 1.4\,\mathrm{mT}$. This results in the energy resolution of 396 eV that was stated above. The maximum transmission angle for this configuration amounts to $\theta_{\mathrm{max}}^{\mathrm{high}} = 68.5°$. However, the low-res scenario achieves magnetic fields of $B_{\mathrm{max}} = 53.6\,\mathrm{mT}$ and $B_{\mathrm{ana}} = 12.4\,\mathrm{mT}$, resulting in the energy resolution of 396 eV and a maximum transmission angle of $\theta_{\mathrm{max}}^{\mathrm{low}} = 69.4°$.
In practice, however, the setup will not only be limited by magnetic retardation but also by other factors such as early retardation or the geometric limitations of the setup which do not allow large flux and cyclotron radii. The impact of these factors on the transmission properties for different configurations will be discussed in section 4.2.3.

2.2. Time-Of-Flight Concepts

A different idea which could potentially serve as an alternative to the standard MAC-E filter is the usage of time-of-flight spectroscopy. This idea has been investigated by [8, 14]. In the following, a short introduction to the general ideas of TOF spectroscopy will be given.
The time it takes for an electron to pass the MAC-E filter depends on its kinetic energy which makes it possible to gather information about the particle's energy from the flight time. This means that it is possible to obtain m_ν^2 as well as all other parameters determining the beta spectrum by measuring the TOF-spectrum. As the flight time $\tau \sim \sqrt{E_\parallel}^{-1}$, it is useful to have a spectrometer such as KATRIN's main spectrometer that can precisely slow down electrons near the endpoint of the beta spectrum which means that TOF measurements of these low-energetic electrons would be very sensitive on small energy differences. Figure 2.3 shows the TOF for electrons in KATRIN with different starting angles and different surplus energies. One can see that for small surplus energies even small energy differences lead to big changes in flight time.
Another advantage of a TOF mode would circumvent the limitation that an integrated spectrum is measured in the standard MAC-E mode. Because of the fact that TOF measurements retain the energy information of single electrons, a differential spectrum is measured. For a fixed retarding potential and a sufficient time resolution it is therefore possible to measure the whole spectrum at once [9].
It can be shown that, given a sufficient time resolution, TOF measurements could lead to an improvement of KATRIN's energy resolution [8]. It is however still unclear how to obtain a start signal from an electron propagating through the spectrometer. As of yet there is no technical realization of an electron tagger that complies with the requirements in sensitivity. Current ideas include the measurement of radiation emitted by an accelerated electron, work done by image charges or by magnetically induced

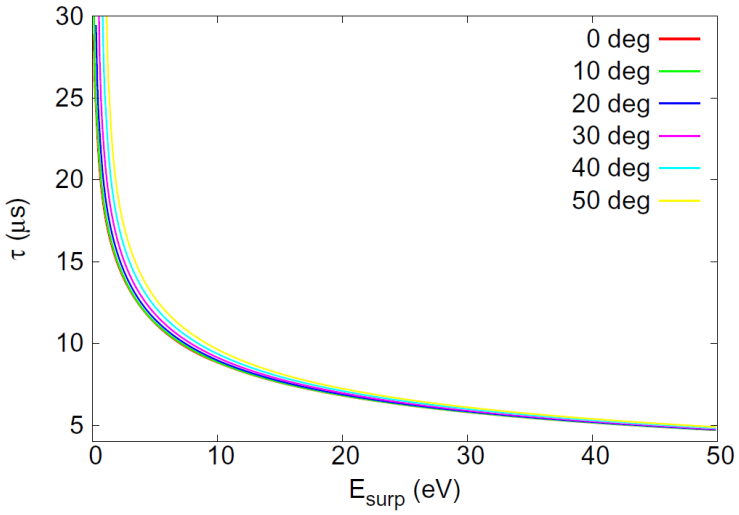

Figure 2.3.: TOF of electrons for different starting angles plotted against the surplus energy $E_{\mathrm{surp}} = E_{\mathrm{kin}} - eU_0$ which shows the $\sqrt{E_{\parallel}}^{-1}$ proportionality [8].

currents flowing through a load circuit and electron-electron interactions. A different method plans to use KATRIN's pre-spectrometer to periodically cut off the electron flux. Simulations show that the gated filtering technique yields a similar statistical uncertainty of $\sigma'_{\mathrm{stat}}(m^2_{\nu_e}) = 0.021\,\mathrm{eV}^2/\mathrm{c}^4$ compared to the uncertainty of the standard MAC-E mode $\sigma_{\mathrm{stat}}(m^2_{\nu_e}) = 0.020\,\mathrm{eV}^2/\mathrm{c}^4$. A more detailed explanation and analysis of the methods presented above can be found in [8]. Overall, however, none of these methods have proven yet to be sensitive enough to improve KATRIN's measurement properties.

A similar approach that doesn't require an active measurement of the start time is

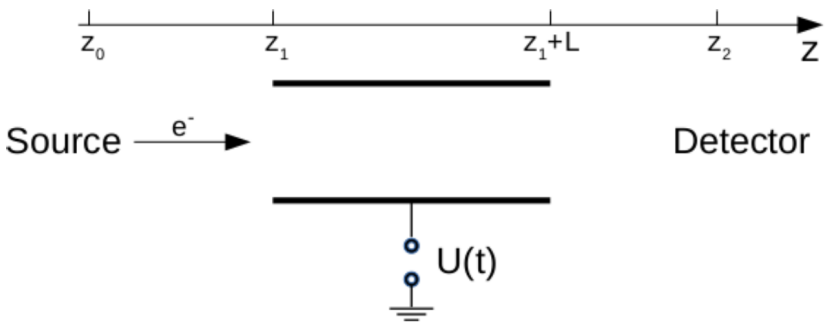

Figure 2.4.: Schematic of a minimalistic tfTOF setup (A. Fulst, personal communication, August 2019).

the time-focusing time-of-flight method which is being developed by A. Fulst [9]. The key feature of a tfTOF setup is a periodically varying electric potential. This can be illustrated with a rather simplistic model which is illustrated in fig. 2.4. It features a drift tube with length L where a time-dependent electric potential $U(t)$ can be applied. Electrons are continuously emitted from a source at z_0, propagate through the drift tube that begins at z_1 and are counted by a detector that also measures the arrival time on the other side of the drift tube at z_2. As electrons arrive at the drift tube, they are accelerated depending on the time they enter the tube. The goal is to control the acceleration process in such a way that, in an ideal case, all electrons with a given energy E_0 and angle θ_0 arrive at the detector at t_{foc}, independent of their start time. It can be shown in a non-relativistic calculation that the time-dependent electric potential for this case can be written as

$$U(t_0) = \frac{1}{e}\left(\frac{m_e L^2}{2\,(t_{\mathrm{foc}} - t_0)} - E_0\right) \tag{2.19}$$

where e is the elementary charge, m_e the mass of an electron and t_0 the start time where the electron enters the drift tube (A. Fulst, personal communication, August 2019). As

$$\lim_{t_0 \to t_{\mathrm{foc}}} U(t_0) \to \infty \tag{2.20}$$

the electric potential needs to be applied in periods $T < t_{\mathrm{foc}}$.
In order to successfully achieve the time-focusing effect, a few aspects need to be kept in mind. Firstly, electron velocities need to be low while the drift tube needs to be long. This maximizes the flight time through the drift tube and thus allows electrons with later start times to be focused on electrons with earlier start times. It also minimizes the effect of the unavoidable parasitic capacitance of the electrode. Furthermore, electron momenta should be collimated as much as possible and the electric field inside the drift tube should be approximately zero which means that the length is much larger than the radius.
All in all the tfTOF method seems to be very promising but needs further investigation. The new TOF setup is designed to be able to test the proposed technique so that the practicality of this method can be evaluated. Eliminating the drawback of measuring an integrated spectrum for neutrino mass measurements would result in additional information that could lead to an increased statistical sensitivity as well as a reduction of systematic uncertainties.

3. TOF Test Setup

In the following, an overview of the TOF measurement setup will be presented. As stated above, it will be used to reduce KATRIN's background and improving its sensitivity by testing different TOF techniques, such as time-focusing time-of-flight.

3.1. Test Rig Design

A general overview of the system can be seen in fig. 3.1. The setup is around 3 m long and consists of an electron source, two spectrometer sections and a detector. First, electrons are emitted via an angular selective electron source, which will be presented in detail in section 3.2. The electrons are then guided through two beam tubes (length 123 cm) that are located symmetrically around a cubic vacuum chamber in the middle of the setup. The cube has vacuum flanges on each side to allow the installation of additional vacuum components e.g. the turbomolecular pump. Electrons reaching the end of the system will enter the detector which outputs a signal to a computer or oscilloscope.
Cylinder electrodes are placed within each beam tube to create the retarding electric field. The electrode length is important as a longer electrode increases the flight time and thus reduces uncertainties concerning the time resolution of the detector. However, an electrode that is too long would lead to an effect called early retardation. This means that electrons with a higher angle wouldn't have fully transformed their transversal energy into longitudinal energy yet. This would impair the angular transmission properties of the spectrometer. There are coils placed at the beginning as well as the end of each beam tube to create the magnetic fields necessary for a MAC-E filter. As the beam tubes are fairly narrow (radius 5.4 cm) an additional coil, directly wound on each beam tube, is required to constrain the flux radius. Since high-voltage feedthroughs and other peripheral devices are needed, there are two CF 40 flanges installed on both beam tubes. As it is not possible to have coil windings around these flanges, one needs to compensate the magnetic field drop by adding further windings in the near proximity of the flange. This will be discussed in detail in section 4.1.

3.2. Angular Selective Photoelectron Source

As the transmission properties of the setup are not comparable to KATRIN's (compare section 2.1.2) it is necessary to investigate electrons with a well-known energy and angle. For this reason a mono-energetic and angular-selective electron source which has been developed in Münster will be used ([15, 12, 16]). Its main features will be presented and

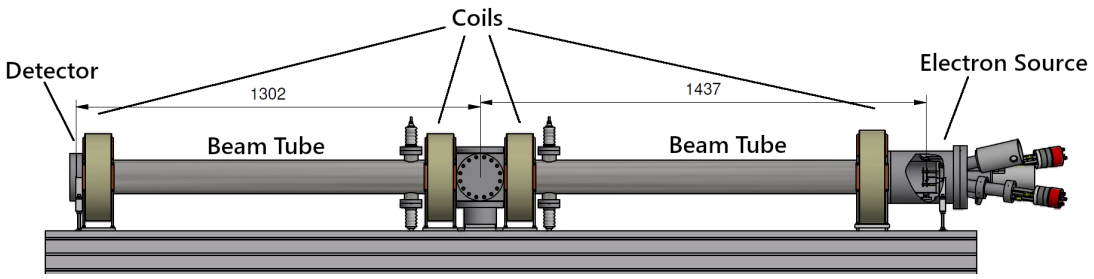

Figure 3.1.: CAD Drawing of the new TOF-test setup (created by H.W. Ortjohann). It features an angular-selective electron source, two beam tubes which include one cylinder electrode each, a chamber in the middle to which the vacuum pump and other additional components will be connected and the detector. Pictures of the partly finished setup are shown in fig. A.1.

discussed briefly in the following section.
A schematic overview of the electron source is presented in fig. 3.2. The main components of the electron source lie inside a grounded cylindrical chamber. Two metal electrodes are placed in the middle of this chamber creating a strong electric field. The backplate is connected to the voltage U_{start} whereas the frontplate is connected to the voltage $U_{\text{start}} + U_{\text{acc}}$. As the power supply of the electron source is connected to a voltage divider with a ratio of 4:3 ($U_{\text{in}} : U_{\text{out}}$) the frontplate voltage is $\frac{3}{4}U_{\text{start}}$ hence the acceleration voltage has a value of $\frac{1}{4}|U_{\text{start}}|$.
Electrons are created at the emission spot P_e via photoelectric effect. For this, light from a UV LED is guided through an optical fiber into the system. The LED is connected to a frequency generator to control the electron emission. A mirror reflects the beam onto a copper single crystal ($\oslash = 1.6\,\text{mm}$) on the backplate. Electrons in the crystal can then absorb a photon and will be emitted from the crystal, when

$$E_{\text{UV}} = h\nu \geq \Phi \tag{3.1}$$

where E_{UV} is the energy of a photon coming from the UV-LED, h is the planck constant, ν the wave frequency and Φ the work function of the material. The starting energy E_{start} of an electron is now determined by

$$E_{\text{start}} = E_{\text{UV}} - \Phi. \tag{3.2}$$

E_{start} directly contributes to the electron energy E_{kin}

$$E_{\text{kin}} = E_{\text{start}} + eU_{\text{start}}. \tag{3.3}$$

Due to this, it is convenient to achieve low starting energies as this effectively also lowers the energy spread of the electron energy. Because of this, a copper single crystal with the work function $\Phi = 4.59\,\text{eV}$ ($E_{\text{UV}} = 4.66\,\text{eV}$) is used.

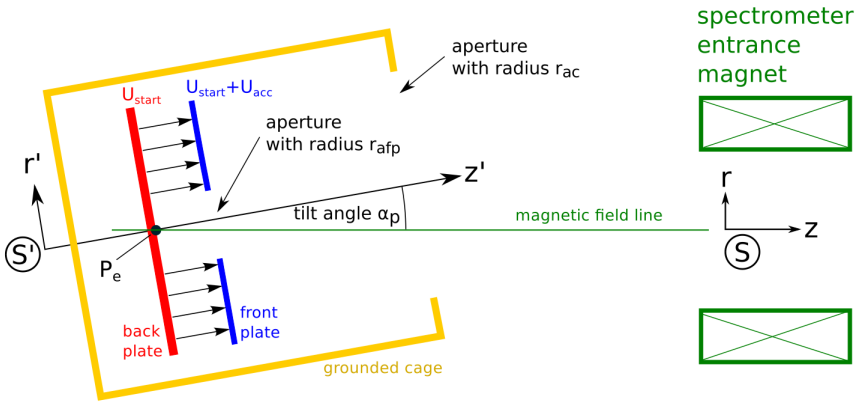

Figure 3.2.: Schematic drawing (not to scale) of the cross-section of the electron source. Two plates are placed inside a cylindrical grounded cage with a distance of 8 mm to each other. The voltage U_{start} is applied to the backplate. The frontplate, however, is set to an acceleration voltage $U_{\text{start}}+U_{\text{acc}}$. The strong electric field between the plates is shown by black arrows. The emission spot P_e is located at the center of the backplate which makes it possible to rotate the source. The angle α_p between the magnetic field and the electron output direction indicates the pitch angle of the electrons. As electrons are accelerated non-adiabatically inside the source-chamber this angle is well-defined. [16]

Between the electrodes, a strong electric field accelerates the emitted electrons non-adiabatically towards the frontplate which they pass through a hole with radius $r_{\text{afp}} = 11.86\,\text{mm}$. The Lorentz force

$$\vec{F_L} = e \cdot (\vec{E} + \vec{v} \times \vec{B}) \tag{3.4}$$

indicates that the electric field $\vec{E}$ is dominant for the movement of the electron between the plates. In the early acceleration phase $\vec{v}$ is small which means that the contribution of the magnetic field $\vec{B}$ is also small. After having passed the frontplate the influence of the electric field decreases. The electrons are now more and more influenced by the magnetic field and start their cyclotron motion around a field line as discussed in section 2.1.
Moreover, the electron source chamber is mounted on a gimbal so that the setup can be rotated around the emission spot. This allows plate angles $\alpha_p > 0$ to be induced (see fig. 3.2). Due to the non-adiabatic acceleration of the electrons this angle is well-defined and can be used to calculate the start angle

$$\theta_{\text{start}} = \arcsin\left(\alpha_p \cdot k \cdot \sqrt{\frac{B_{\text{max}}}{B_{\text{start}}}}\right) \tag{3.5}$$

with the factor k describing the non adiabatic acceleration [15]. For a more in-depth overview of the effects regarding the electron source, refer to [16].

3.3. Electromagnetic Setup

As described above the setup consists of four main coils that are placed at the beginning and the end of each beam tube as well as two assisting coils that are wound onto the beam tube. The main coils are tape coils made of aluminum oxide and are water cooled. The first coil creates the magnetic field B_{start}. In the following it will be referred to as entry coil. The coil is 80 mm long and has 382 windings which results in a thickness of 80 mm. Its core radius is 90 mm.
The other three main coils are manufactured identically with the only difference to the entry coil being the core radius. The core radius is slightly smaller than the entry coil's with 80 cm. This leads to the magnetic field $B_{\text{max}} > B_{\text{start}}$ which induces the effect of magnetic mirroring (see section 2.1) to the system. The number of windings, length and thickness all remain undifferentiated. It is planned to operate these coils at a current of $I_m = 20\,\text{A}$.
Additional coils for the two beam tube sections are necessary to control the electron flux radius. Because of the distance between two main coils, the magnetic field lines would diverge too much so that electrons that do not follow a field line near the center would collide with the tube wall or one of the electrodes. Furthermore, from eq. (2.8) it can be derived that

$$r_{\text{cycl.}} \sim \frac{v_\perp}{B} \tag{3.6}$$

which means that the cyclotron radius increases when lowering the magnetic field. If the magnetic field is too small it might be possible that even electrons following the central field line would collide with the tube wall. To avoid these problems, an assisting coil has been wound onto each of the beam tubes. Enameled copper wire with a diameter of 2 mm is used for both coils. Different currents I_c can be applied to these coils to allow different transmission properties (see section 4.2.3). In principal, the coils should cover the whole length of the tube. However, there are two CF 40 flanges where no wire can be wound (see fig. 3.1). This needs to be taken into account as it creates a drop in the magnetic field. This can potentially cause a magnetic trap that can store electrons in a potential well. To reduce this effect as much as possible, a compensation is necessary. It is designed via magnetic field simulation and will be presented in section 4.1.
The electric retarding potential will be created by two cylindrical electrodes, one in each of the beam tubes. The electrodes feature a length of 0.95 m with a radius of 3.75 cm. Consequently, electric retardation already starts in higher magnetic field regions which will lead to the effect of early retardation. However, as electrons slow down significantly when flying through the electrodes, flight-time will be increased so that the overall sensitivity for TOF measurements will be improved. According to eq. (2.5) slow electrons will also result in a reduced time derivative of the magnetic field. Therefore, an improvement of the adiabaticity is expected.
In fig. 3.3 an exemplary electromagnetic field setup for the low-res setup with $I_c = 20\,\text{A}$ is shown. The curves were simulated with Kassiopeia and show the electric potential as well as the magnetic field that affect an electron propagating on the center field line ($x = y = 0$).

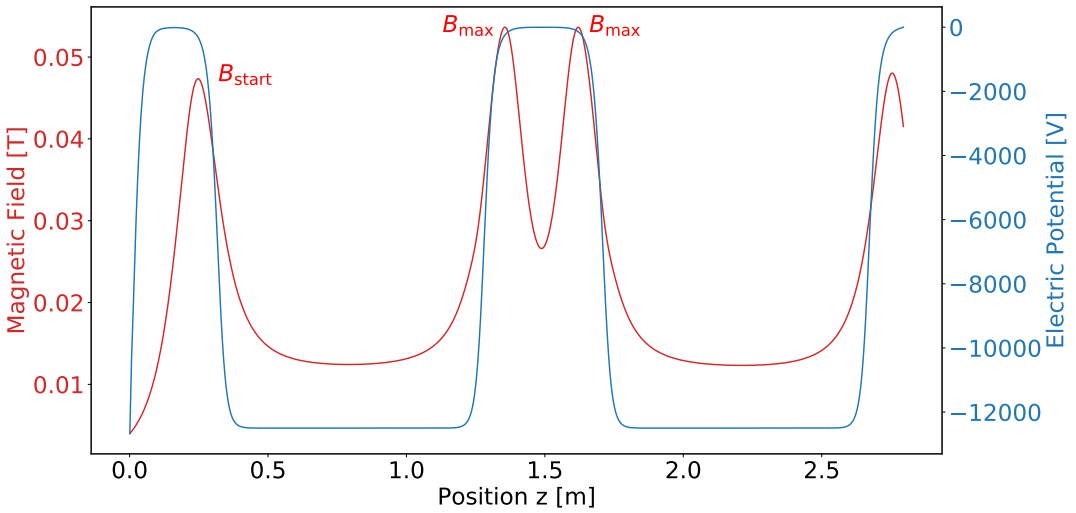

Figure 3.3.: Electromagnetic Setup of the TOF setup. The red curve shows the magnetic field of the low-res setup ($I_c = 20\,\mathrm{A}$) whereas the blue curve shows the electric potential ($U_0 = -13\,000\,\mathrm{V}$).

3.4. Detector

At the end of the system a detector counts the electrons that have passed the system. For the first measurements a windowless Si-PIN photo diode with a size of $18 \times 18\,\mathrm{mm}^2$ is used. This will be replaced later on by a Microchannel Plate (MCP).
The microchannel plate is manufactured by the "tectra GmbH" (specific name of the MCP). MCPs offer many advantages over standard PIN diodes e.g. high efficiency with a good resolution and fast response time. In this case the MCP achieves a response time of $\sim 40\,\mathrm{ns}$ [17]. These properties make them useful in a variety of scenarios such as TOF spectrometry. Incoming electrons will be multiplied in so-called electron tubes (similar to a photomultiplier tube) by a factor that depends on the aspect ratio (fraction length per diameter). With an aspect ratio of 40:1 it is possible to amplify electrons by a factor of over 10.000 [18]. The plate will be mounted inside a vacuum flange to provide an easy installation into the system.
As the MCP is not yet available for use, the Si-PIN photodiode setup from [16] is used for first measurements (Hamamatsu S3204-06). Because the signal output of the Si-PIN diode per electron is relatively low it is directly connected to a preamplifier (Amptec CoolFET A250 CF) outside the vacuum chamber. The detector itself is operated at a bias voltage of 60 V. After further amplification the signal is handed over to a analog-to-digital-converter (ADC). It can then be visualized by an oscilloscope or a computer. With the software MCA Recorder by B. Bieringer [19] the electron spectrum can be recorded. The program assigns the signal to its respective ADC channel which is proportional to the electron's energy.

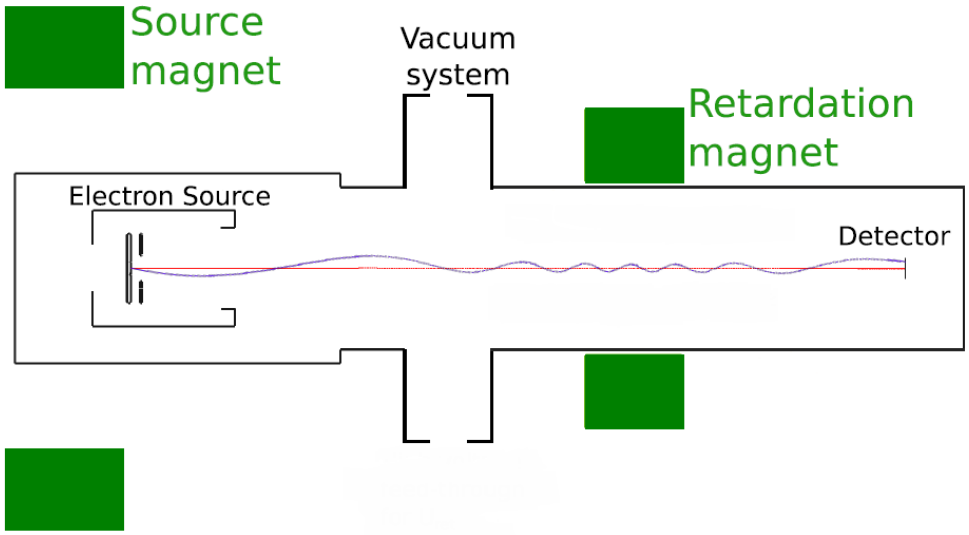

Figure 3.4.: Overview of the electron source test setup (adopted from [16]). On the left, the angular-selective electron source is placed inside a magnetic field created by a water-cooled coil. Electrons are then guided adiabatically to the detector. A further air-cooled coil is placed in front of the detector.

Because of the fact that the electron source has not been used for 2-3 years, it was needed to test the general function of the main components, including the Si-PIN detector. The electron source test setup from [16] as illustrated in fig. 3.4 was used for this. It features the electron source, a water-cooled coil placed around the source, an air-cooled coil in front of the detector and the detector. The water-cooled coil was operated at a current of 80 A whereas a current of 20 A was applied to the air-cooled coil. Electrons with an energy of 13 keV were emitted ($U_{\text{start}} = 13\,\text{kV}$, $U_{\text{acc}} = 3.250\,\text{kV}$). The electron source angle α_p was set to 0.
An exemplary electron spectrum is shown in fig. 3.5. The data of this measurement is dead time corrected. For this, a pulse generator was induced into the system that operated at a frequency of 50 Hz. The difference of the measured counts to the expected value was used to correct for the dead time. The resulting electron spectrum is shown in orange. One can see two peaks of the spectrum. The large first one is called single electron peak whereas the smaller one is the double electron peak. The latter one is the result of two electrons that hit the detector in such a short time frame that the detector effectively sees one electron that deposits twice the energy of a single electron. Other tests have shown that this can also frequently happen with three or more electrons [16]. The count rate of this phenomenon, however, depends on the emission rate of the electrons. Another noticeable effect is that the shape of the single electron peak as well as the background (blue) does not match a gaussian distribution. The background was

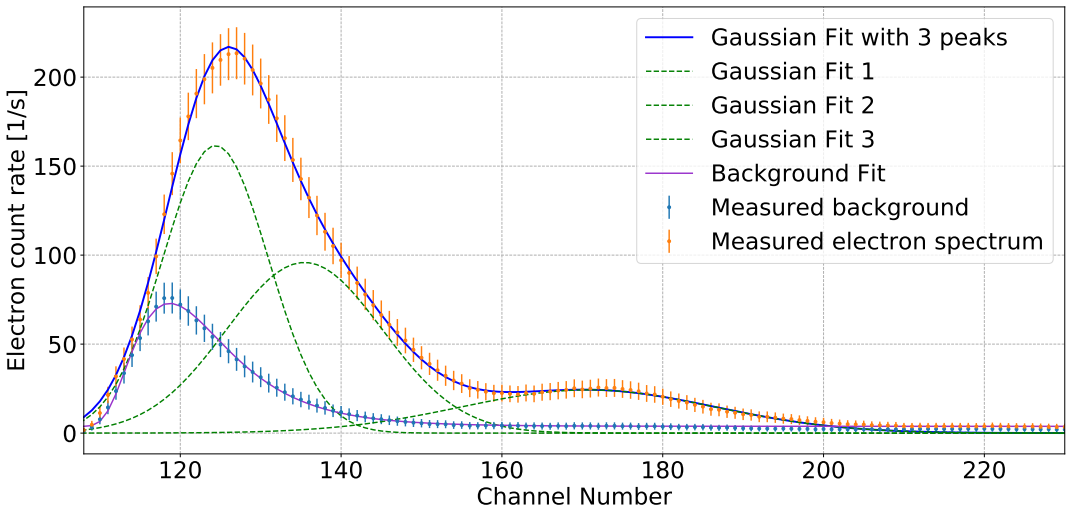

Figure 3.5.: Electron spectrum of the electron source test setup at 13 kV. The measured background (blue) is shown as well as the electron spectrum (orange). The background was fitted with a log-normal distribution (purple line). The complete spectrum was fitted with sum of three gaussian distributions (blue line). Each single gaussian distribution is shown in green.

modeled with a log-normal distribution [20] as this matches the measurement results very well. It is, however, not possible to use this function to model the complete electron spectrum with multiple peaks. To overcome this problem, the single electron peak was fitted with two gaussian distributions. The double electron is suggested to be gaussian distributed hence it can be modeled with a single gaussian. The complete fit with all three functions added together is shown in blue. As one can see, this matches the behavior of the measured electron spectrum very well. The values of the fit parameters as well as the exact fit functions are depicted in the appendix (see tables A.1 and A.2). Nevertheless, it has to be discussed that the measured single electron peak is not gaussian distributed, as it has been shown by [16]. A suggestion to resolve this issue is to operate the electron source at higher voltages so that electrons are emitted with a higher energy. This is briefly mentioned in [16]. If the detector is operated at the settings mentioned above, it can detect electrons with energies above 12 kV. However, it is recommended to use electron energies above 15 kV which helps to fit the electron rate reliably. With this being said, further tests are needed to confirm this behavior.

3.5. Cryogenic Coldhead

As mentioned in section 2.2 there are two approaches to TOF measurements. One of the approaches includes the usage of an electron tagger that detects incoming electrons. A method to extract as little energy as possible from the electron has not yet been fully developed. There are, however, several proposals which all have in common that they can only be operated with superconducting components, thus needing a cryogenic environment. For this reason, a functionality test of a 4 K cryogenic refrigerator has also been done in the scope of this thesis. In the following, the basic principle of pulse tube coolers (PTC) as well as an overview of the functionality of the two stage pulse tube cooler will be given.

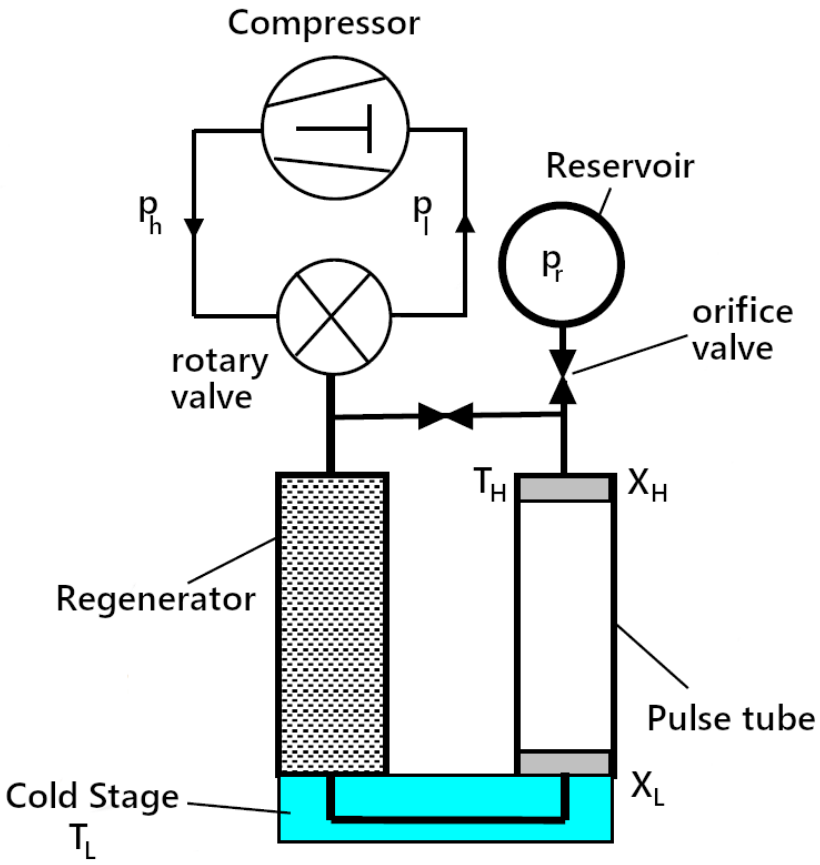

Figure 3.6.: Schematic of a Gifford-McMahon type pulse tube refrigerator. It features a compressor with a high pressure (p_h) and a low pressure (p_l) side. The compressor is connected to a rotary valve that induces a pressure variation inside the system. Adopted from [21].

In 1963 Gifford and Longsworth invented the first refrigerator without moving parts in the low-temperature regions [22]. This was crucial improvement over other cryocoolers as this effectively lowers mechanically induced vibrations and improves longevity. Since then PTCs have developed rapidly hence they are able to achieve much lower temperatures.
Essentially there are two types of PTCs: Stirling-type and Gifford-McMahon-type (GM-type) PTCs with the main difference being the coupling of the compressor to the refrigerator. Stirling-type PTCs are connected directly to the compressor allowing for higher frequencies (30-60 Hz) whereas GM-type PTCs use rotary valves with frequencies in the regime of 0.5-2 Hz [23]. As the 4 K pulse tube cooler used for the setup belongs to the group of GM-type refrigerators the following passage will focus on this type.
A GM-type PTC is sketched in fig. 3.6. It shows the compressor with the two pressure outputs p_h (high pressure) and p_l (low pressure). It is connected to a rotary valve that induces the pressure variation into the system. The cooler itself consists of a regenerator, a pulse tube, two heat exchangers (X_L, X_H), an orifice valve and a reservoir. The regenerator is made up of a porous matrix. Typical regenerator materials include stainless steel or lead. For temperatures below 15 K rare earth materials such as $HoCu_2$ are used [21]. The regenerator can either extract heat from the gas or disperse it again. This is useful as it pre-cools the gas as it flows towards the cold stage X_L. T_H and T_L (high and low temperature) indicate the temperature levels of the heat exchangers. In the first stage of the cooling process the gas is compressed inside the system with the pressure p_h. This causes the gas inside the pulse tube to heat up and flow through the orifice valve ($p_h > p_r$, p_r average pressure in the reservoir) into the reservoir. During that process, it exchanges heat at the warm heat exchanger of the tube X_H, causing the gas to cool down. The oscillation of the rotary valve is set up so that the low pressure side of the compressor is connected to the system right as the gas flow stops, meaning that the pressure inside the tube matches the pressure in the reservoir. When the low pressure side of the compressor is connected to the system, the gas in the pulse tube expands adiabatically, causing it to cool down. As $p_r > p_l$ gas starts to flow out of the reservoir. This leads to a gas flow in the pulse tube towards X_L. Because of the adiabatic expansion in the pulse tube the heat exchanger X_L cools down. Meanwhile, gas inside the regenerator absorbs the heat which it stored there half a cycle ago and cools down again due to the adiabatic expansion. After that, the process repeats [24].
It is important to mention that the pulse tube needs to be long enough so that gas from the warm end (X_H) never reaches the cold end (X_L) and vice versa. The temperature inside the tube then follows a gradient which practically insulates the two ends [24].
The cryocooler used for the setup utilizes this principle as a basis. In this case a two-stage 4 K pulse tube cooler (PTD 406C UHV) by cryo.TransMIT is used. An overview of the main components of the refrigerator can be gathered in fig. 3.8. As the name suggests, it features a two-stage cold head which allows the coldhead to reach temperatures below 4 K at the second stage cold flange. The PTC uses the basic principles of a GM-type PTC described above. In order to further improve the cooling it is designed so that the regenerators are placed sequentially whereas the pulse tubes for both stages are

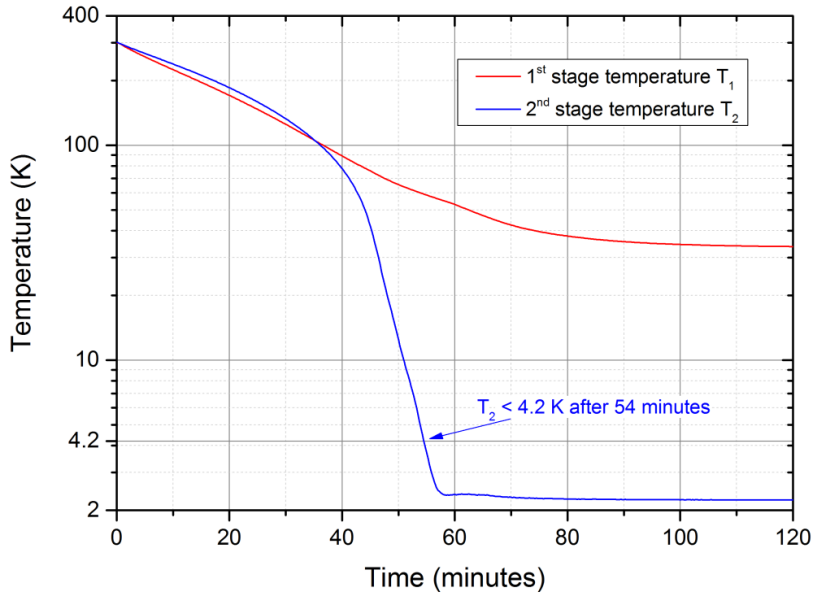

Figure 3.7.: Exemplary temperature curves of the PTD 406C of the cooldown phase for both the first stage cold flange (T_1, red) and the second stage cold flange (T_2, blue) recorded by TransMIT. A SHI F-70H compressor with a filling pressure of 17.5 bar was used for this measurement. This picture was extracted from the user manual [25].

built in parallel. The coldhead is connected via flexlines to a Coolpak 6000 H compressor by Oerlikon Leybold Vacuum which is filled with ^{4}He. The PTC is installed vertically with the second stage cold flange facing downwards to avoid convection inside the pulse tube. The rotary valve is placed separately from the coldhead with a galvanic isolation preventing electric currents to enter the coldhead and potentially disturb the cooling process. Optimally, the PTC is operated with a frequency of 1.2 Hz. A copper radiation shield is installed on the first stage cold flange, surrounding the regenerator and pulse tube of the second stage, as well as the second stage cold flange.
Referring to the manufacturer, the coldhead is able to achieve cooling powers of 10 W @ 42.2 K at the first stage and 0.95 W @ 4.2 K at the second stage [25]. This was tested by TransMIT at their facilities. The temperature curve of that measurement is shown in fig. 3.7. Here, a different compressor was used. The SHI F-70H compressor was operated with a Helium pressure of 17.5 bar (For further information, see [25]). The picture shows the temperature curve for both cooling stages. At first, both curves show nearly no differences. The temperature decreases linearly. After about 40 minutes the temperature of the second stage starts to drop a lot faster than the temperature of the first stage. The target temperature of 4.2 K is reached after about 54 minutes.

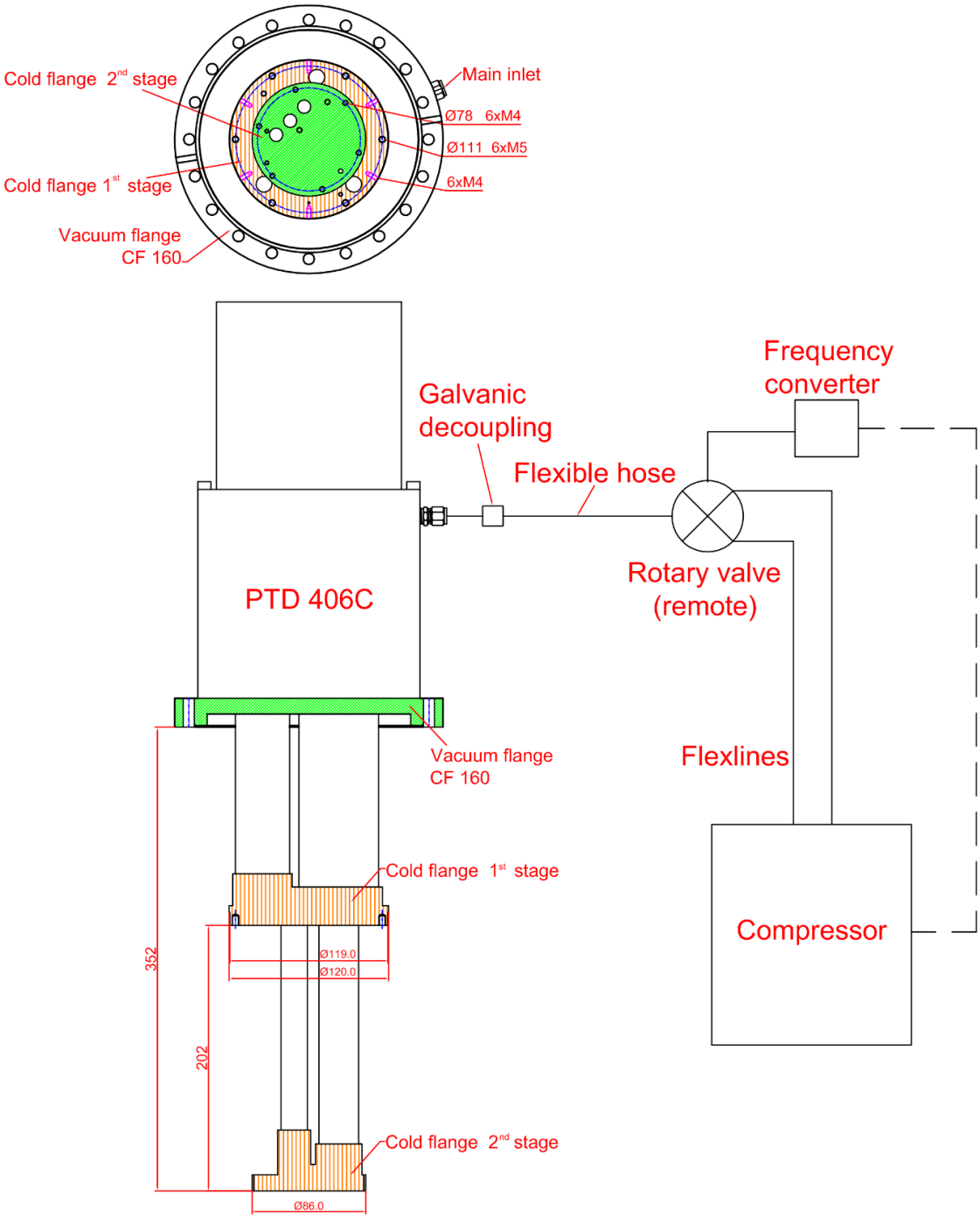

Figure 3.8.: Schematic overview of the 4 K pulse tube cooler (PTD 406C UHV). On the top, the picture shows a topview from underneath the coldhead. A cross-section that shows all the main components is shown below [25].

4. Simulations

To support the development of the setup it is crucial to investigate the physical properties via simulation. Therefore, the following sections will focus on calculations that help to reduce inhomogeneities in the magnetic field as well as particle tracking simulations that investigate the transmission properties of the setup when it is commisioned.

4.1. Magnetic Field Compensation with BField_3D

In previous chapters it was mentioned that enameled copper wire is wound onto the beam tubes to control the flux and cyclotron radius of the electrons. However, there are two CF40 flanges installed which make it impossible to achieve a continuous wiring over the full length of the beam tubes. The created gap leads to a drop in the magnetic field that needs to be compensated. How the compensation needs to be designed will be presented in this chapter. The calculations are done via the simulation software BField_3D [26]. The coordinate system in the simulation is defined so that the z-axis points in the direction of the beam line with $z = 0$ at the start of the beam tube. A single layer of copper wire with a diameter of 2 mm is wound directly around the tube which has a diameter of (107.0 ± 0.2) mm. Wire can be wound from $z = 2$ cm to $z = 8$ cm and from $z = 16.5$ cm to the end of the tube at $z = 121$ cm.
As the magnetic field of a cylinder coil scales linearly with the current it is sufficient to just look at relative magnetic field values $B(z)/B_0$ where B_0 is the maximum value of an ideal magnetic field. The ideal magnetic field would be achieved by a continuous wiring over the full length of the beam tube. Figure 4.1 shows the curves of the relative magnetic field $B(z)/B_0$ for three different cases. The orange line shows the ideal case as mentioned above, the blue line shows the magnetic field without a compensation for the flange and the dashed green line represents the chosen compensation. All three curves are computed for the center of the tube ($x = y = 0$). The restricted area which is 40 mm long and in which no wire can be wound is indicated in blue.
The blue line shows that without a compensation, the magnetic field starts to drop off far before the flange. The local maximum is reached at $z = 8.5$ cm with $B(z)/B_0 = 78.0\,\%$. The deviation from the ideal case is significant. The compensation (green line) has two additional coils added to the setup. The coils are placed symmetrically before and after the flange. They consist of two layers of the same 2 mm thick enameled copper wire and can be wired on top of the existing coil. A total of eleven windings is needed, six windings at the bottom and 5 windings at the top. The resulting magnetic field shows an elevation over the ideal curve at $z = 10$ cm and 20 cm. Compared to the uncompensated magnetic field the drop at $z = 14$ cm is smaller. On average the two elevations and the

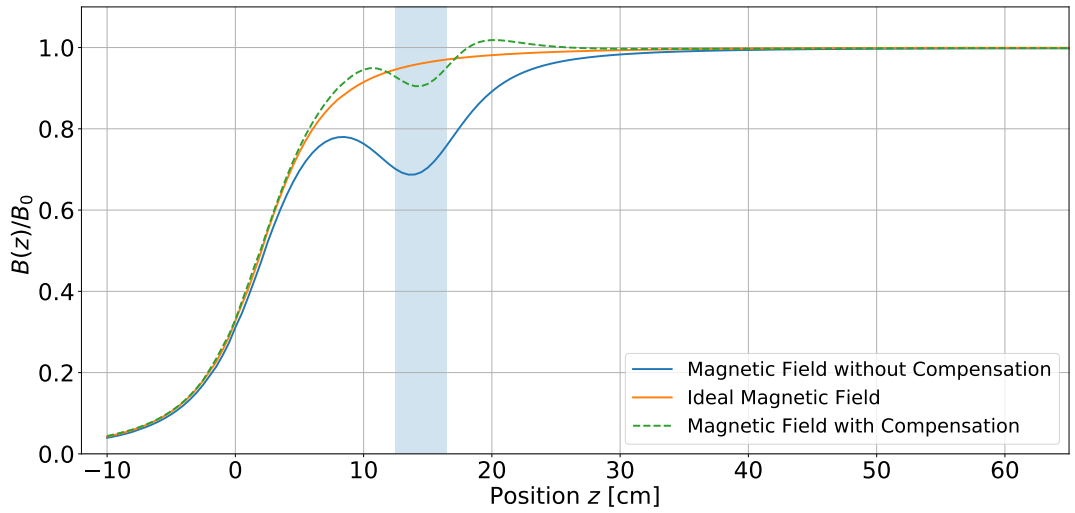

Figure 4.1.: Relative magnetic field $B(z)/B_0$ (B_0 maximum magnetic field in the ideal case) for the ideal (orange), uncompensated (blue) and compensated (green) case plotted against the position on the z-axis. The size of the flange is indicated by the blue area. Only the magnetic field of the coil that is wired around the chamber is shown. Other magnetic field influences that will be present when the setup is fully commisioned are left out.

drop cancel each other out. It must also be noted that this solution was chosen because it is easy to implement as there are, apart from the wire, no additional parts required. With the compensation presented above the magnetic field change over the diameter of the flange has been minimized. This benefits the overall homogeneity of the setup as possible potential wells at the CF 40 flanges are minimized. Although the main coils in close proximity to the CF 40 flanges will dominate the magnetic field at this position, the compensation allows to apply many different settings affecting the electromagnetic setup.

4.2. Particle Tracking with Kassiopeia

For particle tracking simulations the software package Kassiopeia [27] is used. It has been developed within the KATRIN collaboration and allows to simulate tracks in setups that feature high complexity regarding geometry and electromagnetic fields. Its main features and methods that are used for the simulations will be introduced hereinafter, followed by particle tracking simulations that investigate the transmission properties and adiabaticity of the TOF setup.

Kassiopeia

Kassiopeia is developed in C++ and uses the object-oriented programming paradigm. This makes the package applicable not only for the KATRIN experiment but also for a broad variety of experiments that feature different (electromagnetic) designs. Thereby, user input is handled via XML configuration files.
A particle track in Kassiopeia is built of steps that save the evolution of the physical state of the particle over the course of the track. For each step, the equation of motion is solved. At the start of each track, a particle is created by a *generator*. The *generator* defines many start parameters of the particle, such as the particle type, the initial kinetic energy, the starting position and the initial direction of the particle. *Generators* also allow the user to input probability distributions or lists as values for these parameters. A track is completed when a terminating condition (*Terminator*) is fulfilled.
Electromagnetic field calculation is handled by the module *KEMField*. Therein, magnetic fields can either be calculated using direct integration of the Biot-Savart formula or with the zonal harmonic expansion method which only works when the setup is axisymmetrical [28]. Using Legendre polynomials, this method offers fast and accurate calculations. The electric field calculation in Kassiopeia is done by computing charge densities. These are calculated via the boundary element method (BEM). Electric fields can either be computed by direct integration or again by the usage of zonal harmonic expansion [12].

Simulation of the TOF setup

The new TOF setup was implemented into Kassiopeia and is shown in fig. 4.2. It features all the main components. The geometry of the electron source which is shown on the left was created by J. Behrens. For plate angles $\alpha_p = 0°$ the zonal harmonic expansion method is used to calculated the electric field. Tilting of the electron source to change the plate angle α_p is in principle supported. However, the setup then loses its axial symmetry which requires direct integration to compute the electric fields. This demands a lot of processing power which lead to computation times of over 24 hours with greatly reduced sensitivity settings..
As the TOF setup exclusively contains axisymmetric coils, the magnetic field is calculated with the zonal harmonic expansion method. Exact tracking is used during simulations to account for potential violations of the adiabaticity. An increment of $1/60^{\text{th}}$ of a cyclotron period was used because larger step sizes resulted in warnings regarding the terminating condition. Because of that the simulation was significantly slowed down compared to smaller step sizes.

4.2.1. Electron Generation

In order to investigate adiabaticity violations and transmission properties, electrons with a pitch angle of $\theta_{\text{start}} \geq 0°$ are generated. Since tilting the electron source in the simula-

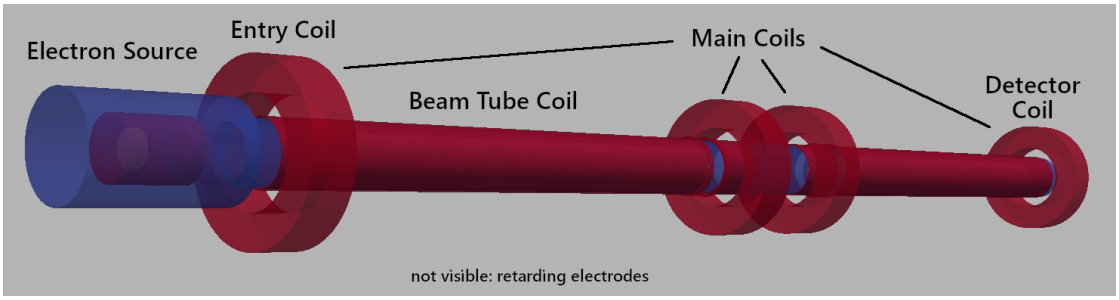

Figure 4.2.: Visualization of the TOF setup in Kassiopeia. The picture is color-coded with coils being colored in red, vacuum chambers (ground potential) blue, retarding electrodes light red. The electron source is located on the left in front of the leftmost coil.

tion would require more computing power a different way to generate particles is needed. As the electron source has already been tested in Kassiopeia [15] electrons are generated within the beam tube at the first coil. Excluding the electron source from the simulation enables to determine angular dependent transmission properties without breaking the axial symmetry. It is convenient to generate particles at this position because the angle θ_{start} is well-defined at this particular position (see eq. (3.5)). Thereby, this angle can directly be used for electron creation in the generator settings.
In fig. 3.3 it can be seen that the electric potential at the center of the entry coil $U(z_{\text{entry}}) \neq 0$ holds. If electrons started at the electron source this potential would decrease the longitudinal energy component. At $z = z_{\text{entry}}$ it is therefore not allowed to create electrons with the energy E_{start}. The energy E_{gen} that is entered in the generator settings must account for $U(z_{\text{entry}})$ by using the difference

$$E_{\text{gen}} = E_{\text{start}} - U(z_{\text{entry}}). \tag{4.1}$$

Figure 4.3 shows that the value of the electric potential at this position depends on the applied retarding potential U_0. In this figure, the initial electric potential which was extracted from Kassiopeia simulations with different U_0 is plotted against U_0. A linear correlation is visible which is why a linear fit $U(z_{\text{entry}}, U_0) = a \cdot U_0 + b$ was done. The fit enables the calculation of

$$E_{\text{gen}} = E_{\text{start}} - U(z_{\text{entry}}, U_0) = E_{\text{start}} - (a \cdot U_0 + b). \tag{4.2}$$

which can then be entered in the generator settings.

4.2.2. Adiabaticity

The following chapter will investigate the orbital magnetic moment μ of electrons propagating through the system. According to section 2.1, μ should remain constant over the course of the system. Three different setup configurations with $I_c = 1\,\text{A}$, $10\,\text{A}$, $20\,\text{A}$ are examined.

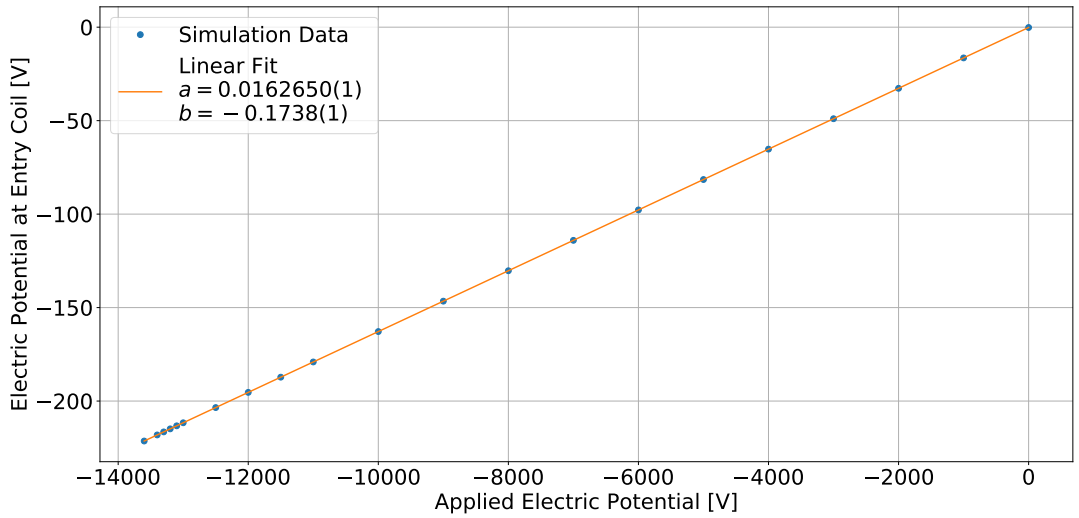

Figure 4.3.: Electric potential inside the entrance coil dependent of the applied electric potential U_0. The parameters of the linear fit are used to determine the start energy when using the generator that lies inside the entrance coil.

Exemplary behaviors of the orbital magnetic moment are illustrated in fig. 4.4. The figure shows the orbital magnetic moment of electrons with different θ_{start} over the course of the whole system. In this case, a retarding potential of $U_0 = -12\,900\,\text{V}$ and $I_c = 10\,\text{A}$ were used. One can directly see that higher angles correspond to higher magnetic moments, thus confirming eq. (2.4). While the curve for $\theta_{\text{start}} = 0°$ scales with $10^{-21}\,\text{Am}^2$, electrons with $\theta_{\text{start}} = 3.3°$ to $\theta_{\text{start}} = 6.7°$ exhibit a magnetic moment in the range of $10^{-16}\,\text{Am}^2$. The magnetic moment shows inhomogeneities at $z = 0.25\,\text{m}$, $1.5\,\text{m}$ and $2.7\,\text{m}$ which correspond with the position of the main coils. Inside the electrodes from $z = 0.3\,\text{m}$ to $z = 1.2\,\text{m}$ and from $z = 1.7\,\text{m}$ to $z = 2.6\,\text{m}$ the curve of the magnetic moment is homogeneous and nearly constant. However, between the left and the right homogeneous section of the setup, there exists a difference of the magnetic moment. After the inhomogeneous region caused by the two coils creating the magnetic field maximums B_{max} (see fig. 3.3, the orbital magnetic moment does not return to its original value in the first electrode resulting in a non-adiabatic motion. The impact of this adiabaticity violation on the time-of-flight $|\Delta\tau|$, the kinetic energy component $|\Delta E_\perp|$ and the angle $|\Delta\theta|$ will be investigated hereinafter. In this case, $|\Delta\tau|$ specifies the difference between the flight times inside the electrodes whereas $|\Delta E_\perp|$ is calculated using the respective maximum of the transversal kinetic energy $E_\perp(z)$ inside either of the electrodes and $|\Delta\theta|$ using the minimum of $\theta(z)$ to gain comparable results.
$|\Delta\tau|$, $|\Delta E_\perp|$ and $|\Delta\theta|$ as a function of the start angle θ_{start} are presented in figs. 4.5 and 4.6 for $I_c = 20\,\text{A}$ and $10\,\text{A}$ and four different retarding potentials ranging from $U_0 = -11\,500\,\text{V}$ to $-12\,900\,\text{V}$. These retarding potentials are chosen to illustrate of what is to be expected from the setup. Higher retarding potentials limit the maximum

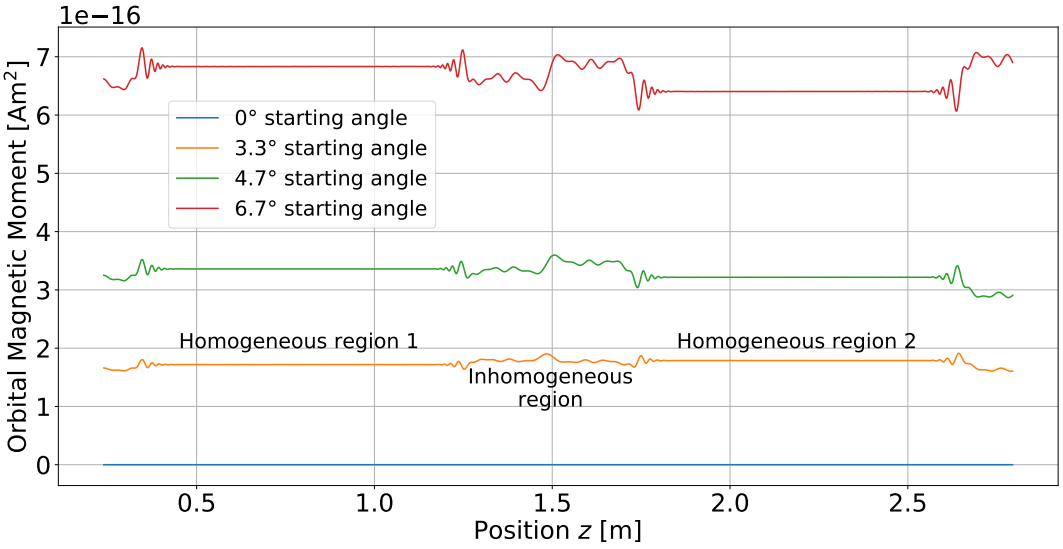

Figure 4.4.: Orbital magnetic moment of electrons with different start angles θ_{start}, $U_0 = -12\,900\,\text{V}$ and $I_c = 10\,\text{A}$.

transmission angle (see section 4.2.3). Hence they are left out as the main objective of this analysis is to illustrate the angular dependency of $|\Delta\tau|$, $|\Delta E_\perp|$ and $|\Delta\theta|$.
Both figures show that the time-of-flight, which is displayed in the top frame, is significantly affected at start angles close to the transmission edge. For small angles $|\Delta\tau|$ lies on the sub-nanosecond scale. Close to the maximum transmission angle, time differences grow faster. Figure 4.5 shows maximum time differences in the range of $10 - 25\,\text{ns}$ while fig. 4.6 exhibits maximum time differences in the range of $5 - 21\,\text{ns}$. The rise of $|\Delta\tau|$ close to the transmission edge is due to the lower longitudinal kinetic energy of electrons inside the electrode compared to electrons with smaller pitch angles. From the bottom frame one can deduce that $|\Delta E_\perp|$ becomes larger with higher pitch angles ranging from sub-eV values for low angles to around 45 eV at angles higher than 20°. Total energy is conserved in the system, hence this amount of energy is transferred to the longitudinal energy component. As $E_\parallel \to 0$ for electrons with high pitch angles inside the first electrode and $E_\parallel \sim v_\parallel^2$, time differences are increased significantly.
Similar to the transversal energy difference, $|\Delta\theta| \to 0$ for start angles $\theta_{\text{start}} \to 0°$. The higher the start angle the larger the possible difference can be with values ranging from 0° to 2° in the case of $I_c = 10\,\text{A}$ or 2.3° with $I_c = 20\,\text{A}$. In fig. 4.6 the curves for $U_0 = -12\,000\,\text{V}$ and $-11\,000\,\text{V}$ exhibit a noticeable sinusoidal shape for $\theta_{\text{start}} < 15°$. As of yet it is unclear what the cause of this effect is. Further simulations need to be carried out to examine the properties of this effect.
Focusing on the configuration with $I_c = 1\,\text{A}$ and $U_0 = -12\,000\,\text{V}$ one ascertains that the region inside the electrodes is no longer homogeneous. Figure 4.8 shows the magnetic

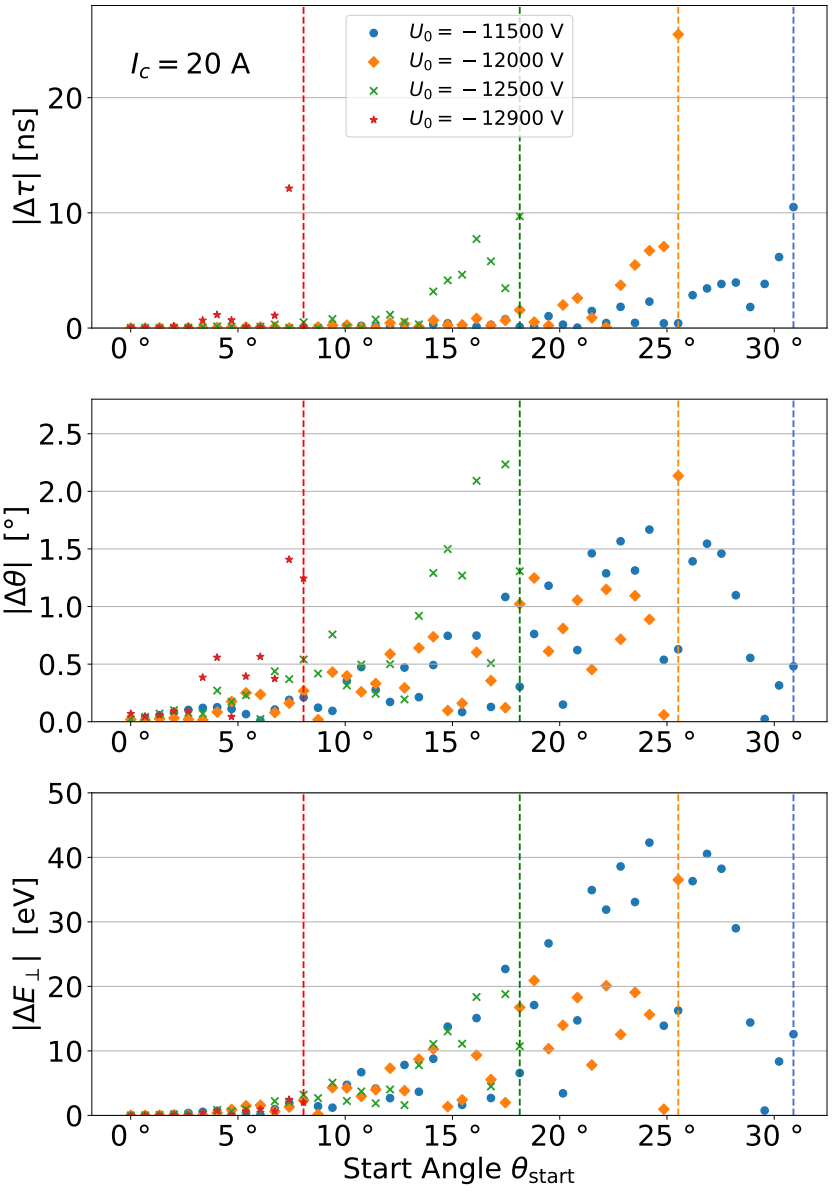

Figure 4.5.: Comparison of $|\Delta\tau|$, $|\Delta E_\perp|$ and $|\Delta\theta|$ of an electron between the two electrodes for three different retarding potentials U_0 and $I_c = 20\,\text{A}$ as a function of the angle θ_{start}. The vertical lines indicate the maximum transmitted angle as presented in section 4.2.3.

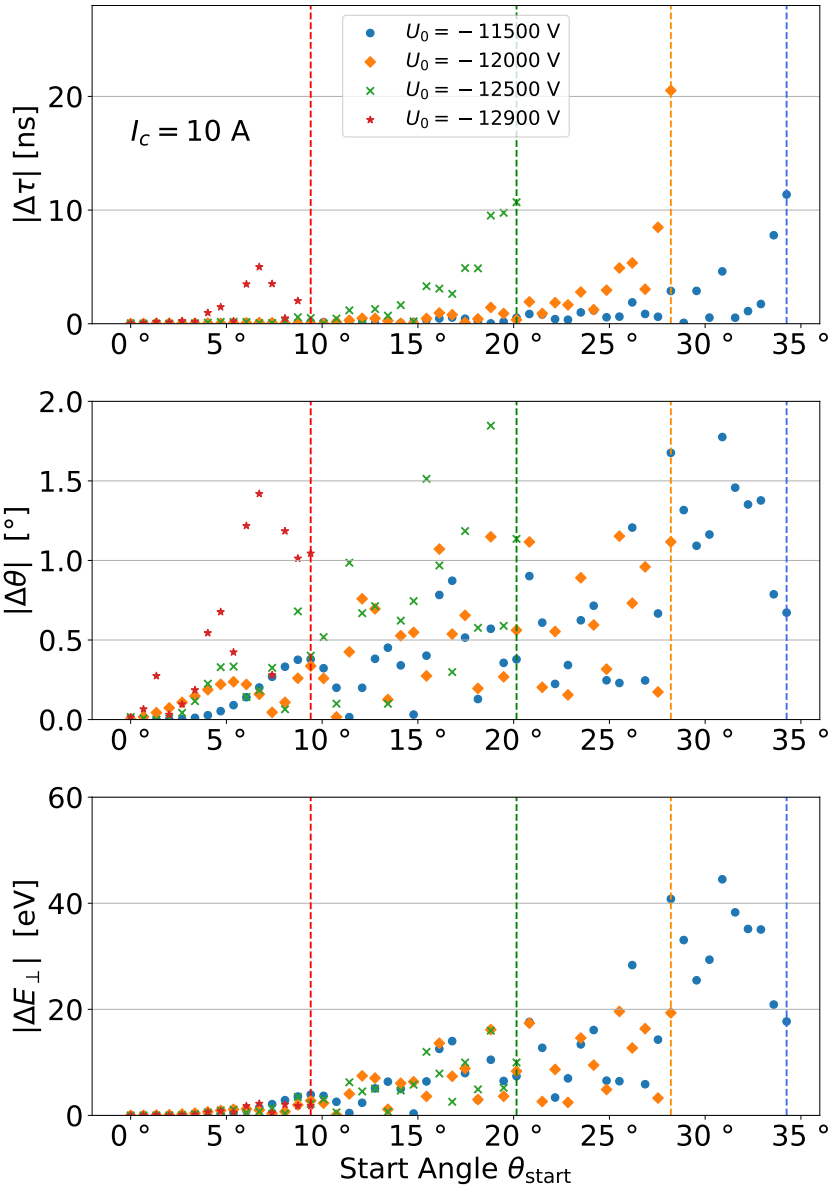

Figure 4.6.: Comparison of $|\Delta\tau|$, $|\Delta E_\perp|$ and $|\Delta\theta|$ of an electron between the two electrodes for three different retarding potentials U_0 and $I_c = 10\,\text{A}$ as a function of the angle θ_{start}. The vertical lines indicate the maximum transmitted angle as presented in section 4.2.3.

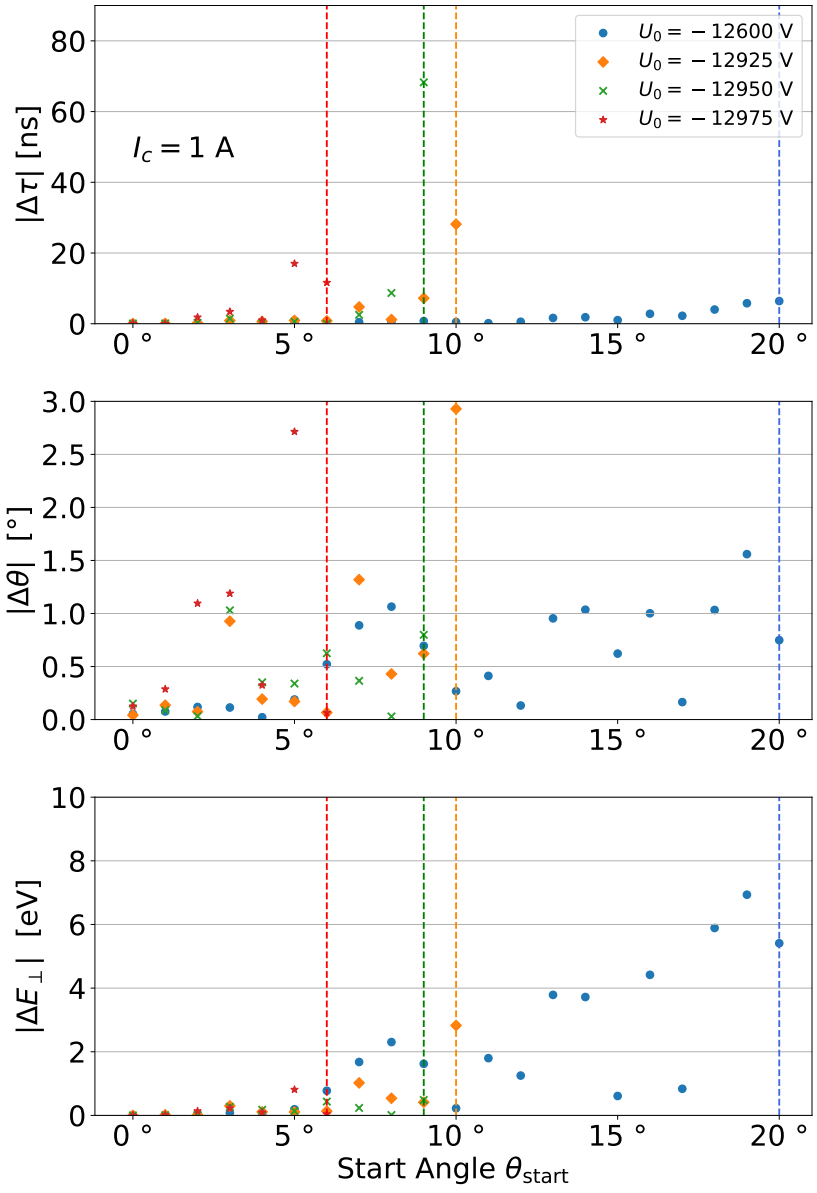

Figure 4.7.: Comparison of $|\Delta\tau|$, $|\Delta E_\perp|$ and $|\Delta\theta|$ of an electron between the two electrodes for three different retarding potentials U_0 and $I_c = 1\,\text{A}$ as a function of the angle θ_{start}. The vertical lines indicate the maximum transmitted angle as presented in section 4.2.3.

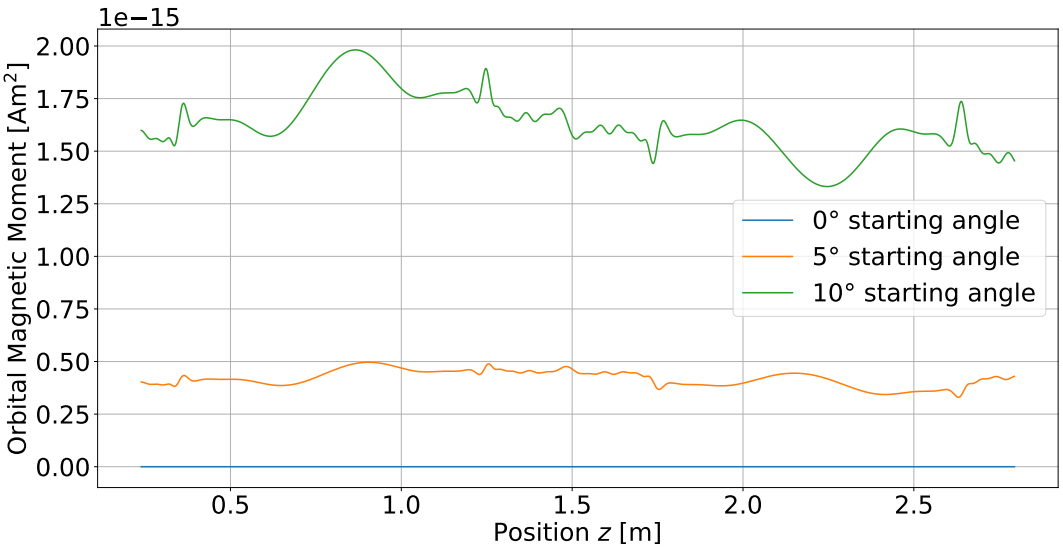

Figure 4.8.: Orbital magnetic moment of electrons with different start angles θ_{start}, $U_0 = -12\,000\,\text{V}$ and $I_c = 1\,\text{A}$.

moment of electrons traveling through the system with this magnetic configuration. One can see that there is a change of μ inside the electrode which is of the same magnitude as the difference investigated before. Simulations with $I_c = 10\,\text{A}$ and $20\,\text{A}$ also revealed this behavior for electrons with large surplus energies.
The impact of the change of the magnetic moment at the middle of the setup with $I_c = 1\,\text{A}$ is illustrated in fig. 4.7. Due to the adiabaticity violations inside the electrodes at large surplus energies, the figure only shows data from runs with $U_0 \leq -12\,600\,\text{V}$. All three plots show similar behaviors compared to the ones presented before. Time differences close to the transmission edge range up to $70\,\text{ns}$ while differences of θ are possible up to 3° with the majority being in the range of 0° to 2°. Values for $|\Delta E_\perp|$ are smaller in comparison to larger I_c as $7\,\text{eV}$ is not exceeded below $\theta_{\text{start}} = 20°$.

In conclusion, the orbital magnetic moment μ of an electron traveling through the system is impacted by the magnetic field change in the middle of the system between both beam tubes. The direction of this change is inconsistent which means that μ may increase or decrease when passing the region between $z = 1.3\,\text{m}$ and $z = 1.7\,\text{m}$. By calculating the change of the time-of-flight τ, the angle θ and the difference of the transversal energy component $E_\perp$ between the homogeneous regions inside the electrodes one can see that the absolute change of these parameters depends on the start angle θ_{start} and in case of θ and τ also on the surplus energy. For each specific measurement, this data can be used to determine which setup configuration is most suited. It is also important to adjust the retarding potential U_0 in correspondance with the chosen current I_c. Fast electrons exhibit adiabaticity violations even inside the electrodes which can significantly impact

the particular measurement. The surplus energies at which these violations occur are correlated to I_c, meaning that with smaller I_c the surplus energy needs to be smaller to avoid these non-adiabatic effects.

4.2.3. Transmission Properties

In the following section simulation results regarding the transmission properties of the TOF setup will be presented. Simulations were done again for three different currents $I_c = 1\,\mathrm{A}$, $10\,\mathrm{A}$ and $20\,\mathrm{A}$ and electrons were generated at the center of the entry coil with a total energy $E_{\mathrm{start}} = 13\,\mathrm{keV}$. Each simulation run was done with a specific retardation voltage ranging from $-13200\,\mathrm{V}$ to $0\,\mathrm{V}$. The angular transmission properties were simulated using a list of angles from $0°$ to $70°$ with a step size of $0.7°$. The last electron that reached the end of the setup defines the maximum transmitted angle. For the transmission probability a total number of $N = 2000$ electrons was simulated in each run. These electrons were generated using an angular distribution of an isotropically emitting source. The transmission probability is defined by the ratio of transmitted electrons to the total number of electrons N.

Magnetic Field Configuration $I_c = 20\,\mathrm{A}$

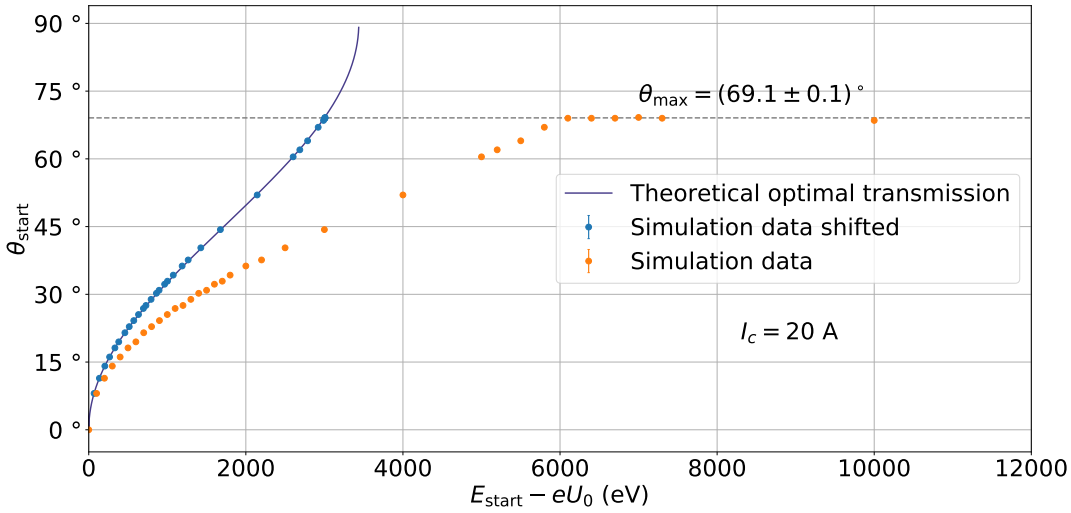

Figure 4.9.: Angular transmission of the setup with $I_c = 20\,\mathrm{A}$. It shows the maximum transmission angle which is affected by early retardation. The shifted data points eliminate this effect and show that the data is compatible with the theoretical angular transmission. A maximum transmission angle of $\theta_{\mathrm{max}} = (69.1 \pm 0.1)\,°$ is reached at an estimated surplus energy $E_{\mathrm{start}} - eU_0 > 6\,\mathrm{keV}$.

The angular transmission properties of the setup with $I_c = 20\,\mathrm{A}$, which was depicted

as the low-res setup in section 2.1 is shown in fig. 4.9. It shows the maximum transmitted angle θ_{max} for each surplus energy $E_{\text{start}} - eU_0$. For reference the ideal function for θ_{max} from eq. (2.17) which only takes magnetic retardation into account is also depicted in the picture (blue curve). The simulation data (orange curve) shows a clear deviation from the ideal case. The data is shifted to higher surplus energies and the higher the surplus energy the larger the deviation from the optimal transmission curve. This leads to the effective energy resolution $\Delta E_{\text{eff}} \approx 6\,\text{keV}$ which is twice the value of the energy resolution in the ideal case. However, the mean of all maximum transmission angles at surplus energies $> \Delta E_{\text{eff}}$ yields $\theta_{\text{max}} = (69.1 \pm 0.1)\,^\circ$ which is in accordance with the expected value of $69.4\,^\circ$.

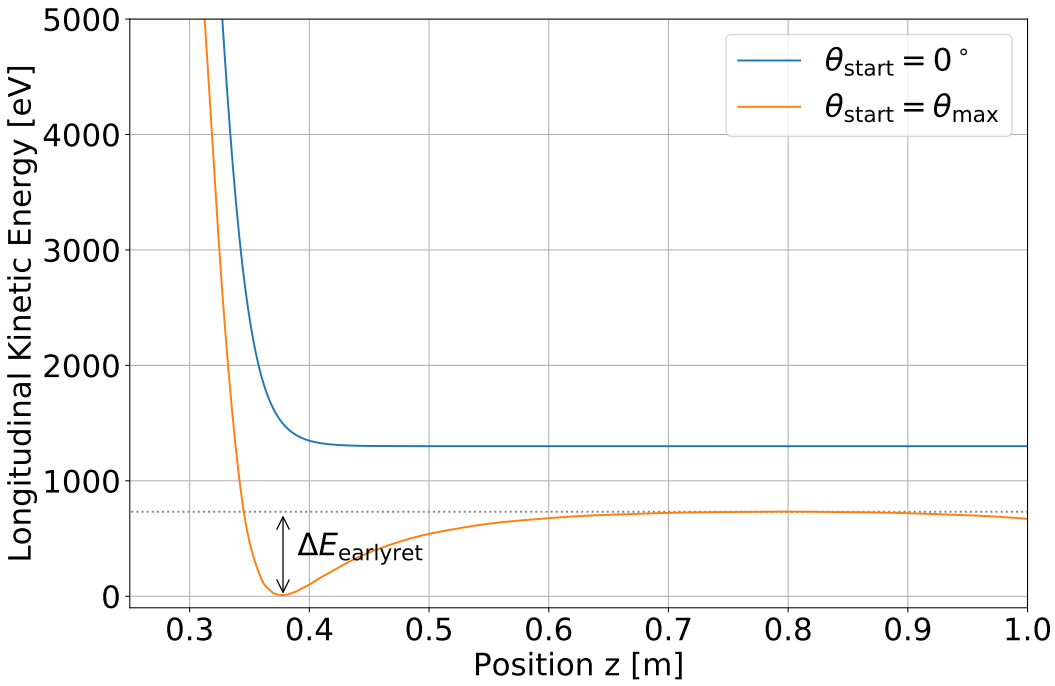

Figure 4.10.: Curves of the longitudinal kinetic energy component at the first beam tube with $U_0 = -11\,700\,\text{V}$ illustrating the effect of early retardation. Electrons with $E_{\text{start}} = 13\,\text{keV}$ and different start angles θ_{start} are simulated. The curve for $\theta_{\text{start}} = 0°$ is not affected by early retardation. The electron with $\theta_{\text{start}} = \theta_{\text{max}}$ is nearly reflected. The energy difference $\Delta E_{\text{earlyret}}$ between the longitudinal energy at the middle of the electrode and the x-axis is used for the correction of the data points in the transmission function.

It was found out, that the deviation is caused by the effect of early retardation which happens if electric retardation takes place before the analysing plane where the magnetic field reaches its minimum. This effect is illustrated in fig. 4.10. The figure displays two

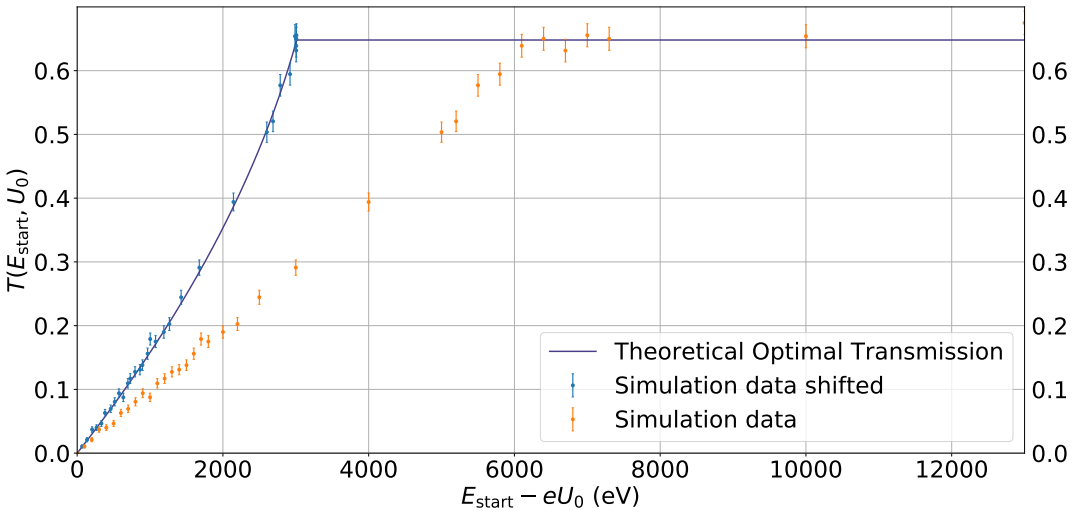

Figure 4.11.: Transmission function of the setup with $I_c = 20\,\text{A}$. It shows the transmission probability taken from simulations with $N = 2000$. The data is affected by early retardation. The shifted data points eliminate this effect and show that the data is compatible with the theoretical transmission. Maximum transmission can be reached at an estimated surplus energy $E_{\text{start}} - eU_0 > 6\,\text{keV}$.

different curves (blue: $\theta_{\text{start}} = 0°$, orange: $\theta_{\text{start}} = \theta_{\text{max}}$) of the longitudinal kinetic energy at the entrance of the first beam tube. Comparing both curves one can see that the orange curve shows a large drop of the longitudinal energy at $z \approx 0.38\,\text{m}$ which is not visible for the $\theta_{\text{start}} = 0°$ electron. This is the result of early retardation. It creates a barrier for electrons with higher angles which would have normally been transmitted. For $\theta = \theta_{\text{max}}$ the minimum energy $E_{\parallel,\text{min}}$ approaches 0 so that the energy difference $\Delta E_{\text{earlyret}}$ can be written as

$$\Delta E_{\text{earlyret}} = \lim_{E_{\parallel,\text{min}} \to 0} E_{\parallel}(\theta_{\text{max}}, z_{\text{ana}}) - E_{\parallel,\text{min}}(\theta_{\text{max}}) = E_{\parallel}(\theta_{\text{max}}, z_{\text{ana}}) \tag{4.3}$$

where z_{ana} is the z-coordinate of the analysing plane. The obtained value can then be used to project the respective maximum transmission angle onto the ideal transmission curve. This is also shown in fig. 4.9. The blue points depict the maximum transmission angle if the setup would not have the effect of early retardation. Unlike the raw simulation data which shows $\theta_{\text{max}}(E_{\text{start}} - eU_0)$ the shifted data is obtained by $\theta_{\text{max}}(E_{\text{start}} - eU_0 - \Delta E_{\text{earlyret}})$ which shifts the data to the left. The resulting data points fit the ideal transmission curve very well which confirms the assumption that the setup is affected by early retardation.

Figure 4.11 shows the transmission probability $T(E_{\text{start}}, U_0)$ for various surplus energies of the low-res setup. Comparison with the theoretical transmission function shows the

same properties as seen in fig. 4.9. The simulation data is again shifted towards higher surplus energies which confirms the effective energy resolution of $\Delta E_{\mathrm{eff},\,20\,\mathrm{A}} \approx 6\,\mathrm{keV}$ mentioned above. Using $\Delta E_{\mathrm{earlyret}}$ from eq. (4.3) the data can also be projected onto the ideal transmission function which shows that the shift is primarily induced by early retardation.

Magnetic Field Configuration $I_c = 10\,\mathrm{A}$

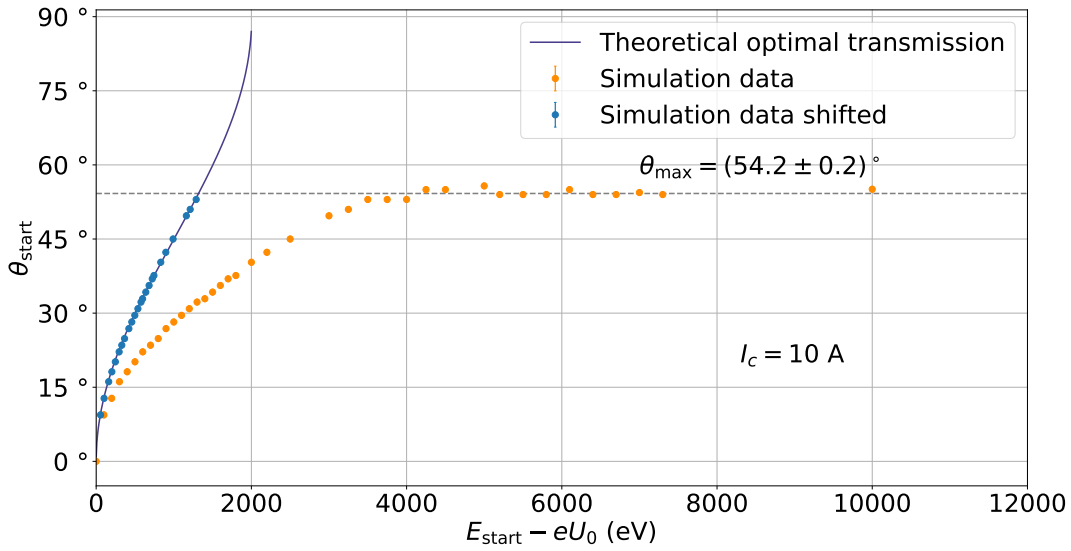

Figure 4.12.: Angular transmission of the setup with $I_c = 10\,\mathrm{A}$. It shows the maximum transmission angle which is affected by early retardation and the electrons hitting the surface of the first electrode. The correction for early retardation is applied for data points which are only affected by early retardation. A maximum transmission angle of $\theta_{\mathrm{max}} = (54.2 \pm 0.2)\,°$ is reached at an estimated surplus energy $E_{\mathrm{start}} - eU_0 > 3.5\,\mathrm{keV}$.

The transmission properties of the setup with $I_c = 10\,\mathrm{A}$ are depicted in figs. 4.12 and 4.13. In theory (see eqs. (2.17) and (2.18)), this setup offers a better energy resolution than the low-res setup with $\Delta E = 1749\,\mathrm{eV}$. This arises from the magnetic field values $B_{\mathrm{start}} = 43\,\mathrm{mT}$, $B_{\mathrm{ana}} = 7\,\mathrm{mT}$ and $B_{\mathrm{max}} = 49\,\mathrm{mT}$. The maximum angle remains almost the same with $\theta_{\mathrm{max}} = 69.1\,°$.
For surplus energies up to 3500 eV both curves show the same general behavior as presented above for $I_c = 20\,\mathrm{A}$. Early retardation causes a shift of the data points to higher surplus energies which can again be shown by eliminating the energy offset. The shifted data points model the ideal transmission function very well in both pictures. At higher surplus energies the curves show no inclination which means that maximum transmission is achieved. The effective energy resolution can be estimated to $\Delta E_{\mathrm{eff},\,10\,\mathrm{A}} \approx 3.5\,\mathrm{keV}$

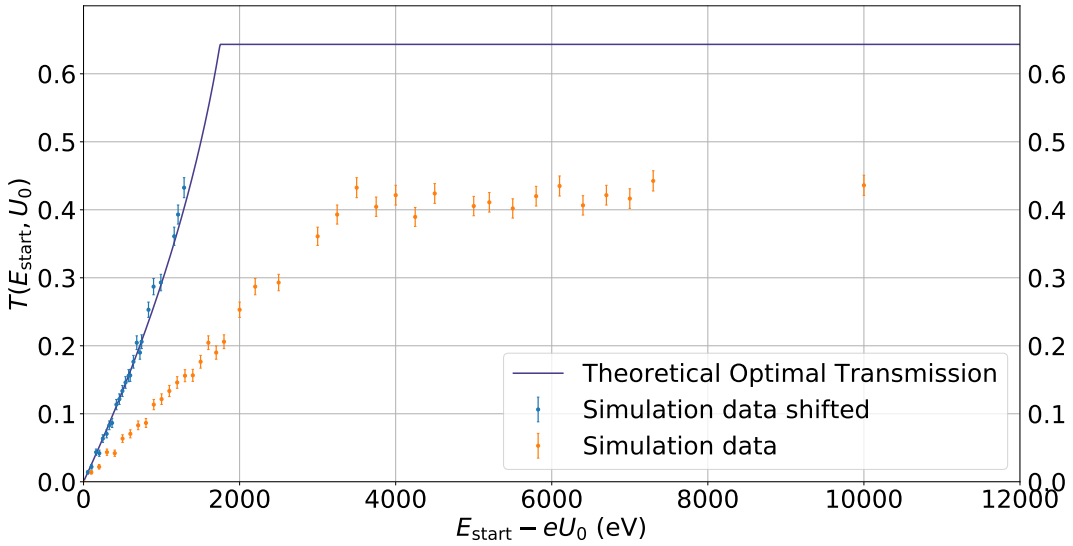

Figure 4.13.: Transmission function of the setup with $I_c = 10\,\text{A}$. It shows the transmission probability taken from simulations with $N = 2000$. The data is affected by early retardation and the electrons hitting the surface of the first electrode. The correction for early retardation is only applied for data points which are only affected by early retardation. Maximum transmission can be reached at an estimated surplus energy $E_{\text{start}} - eU_0 > 3.5\,\text{keV}$.

which is again approximately twice the expected energy resolution. However, it is notable that in fig. 4.12 the expected maximum transmission angle is not reached. In this case a value of $\theta_{\text{max}} = (54.2 \pm 0.2)\,^\circ$ was simulated. This indicates that a new limiting factor is affecting the system. From the used terminating conditions of the corresponding tracks it can be concluded that electrons are stopped inside the first electrode by hitting the electrode's surface. Comparing to the configuration with $I_c = 20\,\text{A}$, the magnetic field at the analysing plane is significantly lower. This causes the electron flux radius as well as the cyclotron radius to increase so that electrons with high angles reliably hit the surface of the electrode. The correction for early retardation is not applicable in this case as it is not possible to retrieve $\Delta E_{\text{earlyret}}$ from simulation data. Because of this, the correction is only applied to data points where the simulation run was purely affected by early retardation.

Magnetic Field Configuration $I_c = 1\,\text{A}$

The third configuration lowers the current to $I_c = 1\,\text{A}$. The theoretical transmission properties of this high-res setup were presented in section 2.1. The simulated angular transmission of this configuration is shown in fig. 4.14a which focuses on the surplus energies from 0 to 1000 eV and fig. 4.14b which also shows larger surplus energies. In the

former picture one can see that electrons up to a surplus energy of 200 eV are affected by early retardation. The shifted data points confirm this correlation as they fit the ideal transmission curve very well. Higher surplus energies do not lead to an increased $\theta_{\max}$. From the simulation output it can be seen that electrons with higher angles hit the surface of the electrode due to the increased flux and cyclotron radius. The maximum transmission angle up to 1000 eV is $\theta_{\max} = (19.1 \pm 0.3)^\circ$ which is significantly smaller than the expected value of $\theta_{\max}^{\text{high}} = 68.5^\circ$. But the effective energy resolution $\Delta E_{\text{eff}} \approx 300\,\text{eV}$ is comparable to the expected value due to the very small maximum transmission angle.
However, according to section 4.2.2 the electron motion shows large adiabaticity violations at higher surplus energies. As the lack of adiabaticity leads to an unpredictable transfer of longitudinal to transversal kinetic energy and vice versa, this likely causes the unpredictable behavior of the curve in fig. 4.14b which shows the angular transmission for higher surplus energies. It is therefore recommended to use this setting only for surplus energies $< 500\,\text{eV}$ to avoid unwanted effects resulting from adiabaticity violations.

In conclusion, the presented configurations show different transmission properties by varying the current I_c of the coils wound around the beam tubes. Each configuration is thereby affected by one or more factors that further limit the transmission apart from magnetic reflection. The transmission properties of the low-res setup with $I_c = 20\,\text{A}$ are only limited by early retardation. This allows angles up to $(69.1 \pm 0.1)^\circ$ to be transmitted at a surplus energy of over 6 keV which makes it useful for the testing of background reduction methods that need a high angular transmission but do not necessarily rely on slow electrons.
By contrast, the high-res setup with $I_c = 1\,\text{A}$ offers an effective energy resolution of around 300 eV with a small maximum transmission angle of $(19.1 \pm 0.3)^\circ$. At surplus energies above 1 keV this configuration is strongly affected by adiabaticity violations which makes the behavior of the electrons in the system unpredictable. At lower surplus energies the angular transmission is limited by the increased flux and cyclotron radius which causes the electrons to collide with the first electrode and again by early retardation. This setup might be useful for scenarios where slow electrons with low surplus energies are needed such as TOF methods.
A good balance between the two configurations offers the setup with $I_c = 10\,\text{A}$. It has a maximum transmission angle of $(54.2 \pm 0.2)^\circ$ at surplus energies $> 3.5\,\text{keV}$. As high surplus energies impair the adiabaticity of the system it is recommended to minimize the surplus energy whenever possible. Therefore, this setup provides a relatively good compromise between high angular acceptance and low surplus energies.
This goes to show that all configurations are useful for specific measurement scenarios and it is of course also possible to chose a different value for I_c to optimize the configuration for the respective measurement.

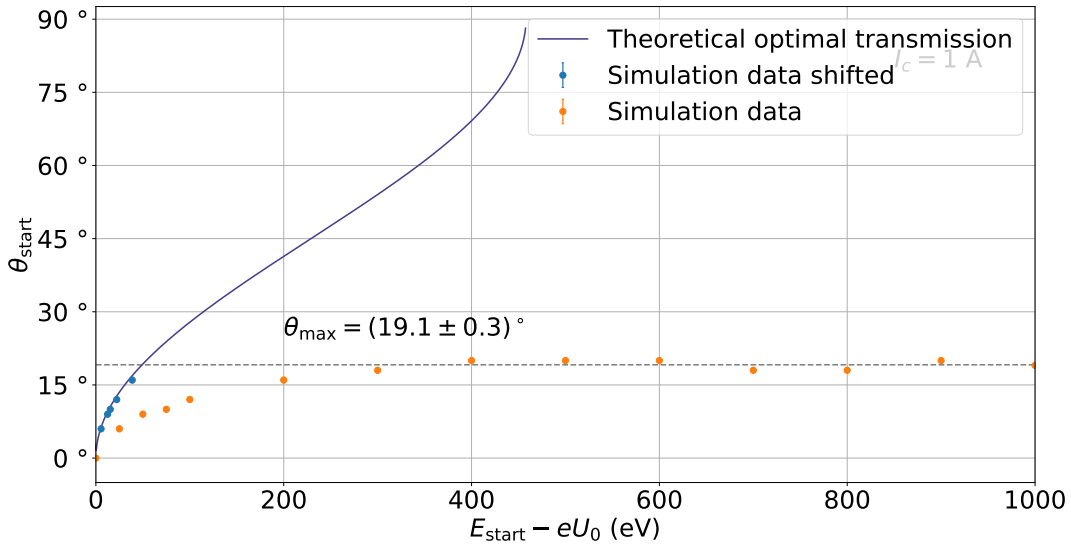

(a) Surplus energies from 0 to 1000 eV. A maximum transmission angle of $\theta_{\text{max}} = (19.1 \pm 0.3)\,^\circ$ is reached at an estimated surplus energy $E_{\text{start}} - eU_0 > 300\,\text{eV}$.

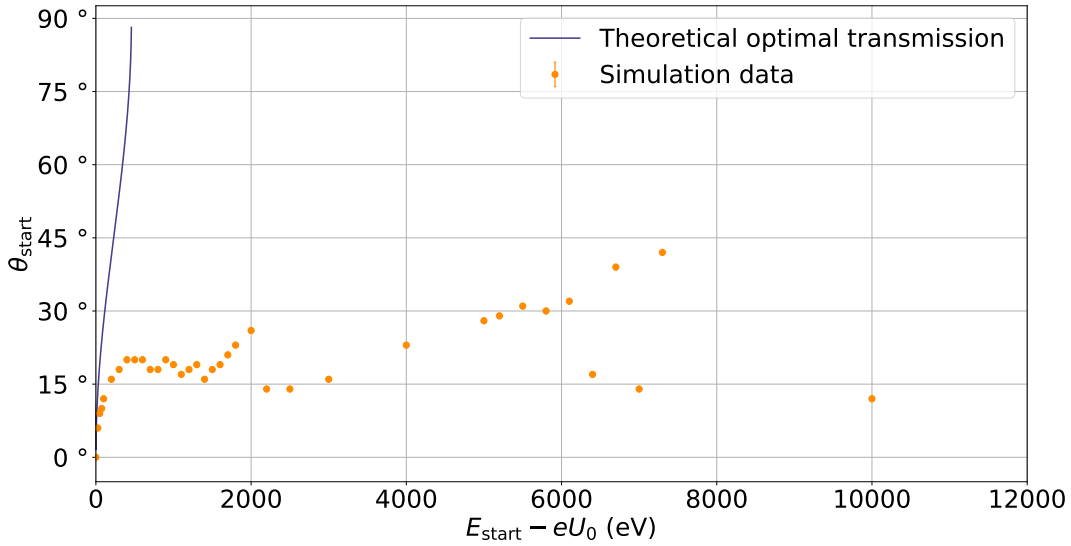

(b) Surplus energies from 0 to 10000 eV.

Figure 4.14.: Angular transmission functions of the setup with $I_c = 1\,\text{A}$.

5. Coldhead Measurements

Current proposals for electron tagger devices include the use of superconducting components. To achieve superconductivity a cryogenic environment is needed. This will be achieved by a helium based two-stage 4 K pulse tube cooler (PTD 406C UHV) by cryo.TransMIT. Results from early test measurements as well as the realization of the temperature readout will be presented in the following chapters.

5.1. Temperature Readout with LabView

The temperature readout of both stages of the coldhead is done by measuring the resistance of negative temperature coefficient (NTC) resistors. For this, a small, well-known electric current is applied to each of the sensors. The voltage drop is then measured by a NI USB-6008 data acquisition (DAQ) device by National Instruments. It serves as an analog-to-digital converter (ADC) and transmits the signal via USB to a computer. The signal is processed by a LabView program (see fig. 5.1) which also controls the DAQ device.
To calculate the temperature, the program obtains the mean value of 2000 voltage measurements and converts it into a resistance value using Ohm's law. The current applied to the circuit must be entered manually via the *Front Panel*. The software then uses the built-in *Lookup Table* method which is available in a *Control & Simulation Loop* to calculate the temperature. If the sensor calibration has previously been imported from a text file the *Lookup Table* method can calculate the temperature value using linear interpolation (or extrapolation). The acquired data is eventually presented on the *Front Panel* and is also written into a text file which can be saved on the computer for later analysis of the data.
The program also allows the usage of a LakeShore Temperature Controller Model 331. As it does all the calculations internally, only the temperature can be displayed on the front panel. The temperature readout process of this device essentially matches the one used in the LabView software. However, the LakeShore device also continuously measures the current which is currently not possible with the LabView program.

5.2. Measurement Results

The first measurement of the cooling process of the coldhead is presented in fig. 5.2. It shows the temperature curve measured at the second stage cold flange by a TVO Tmi-CSS-D3-1340 sensor. The sensor was put inside a copper shield which was attached to the second stage cold flange to optimize heat flow. Teflon cables with a cross section of

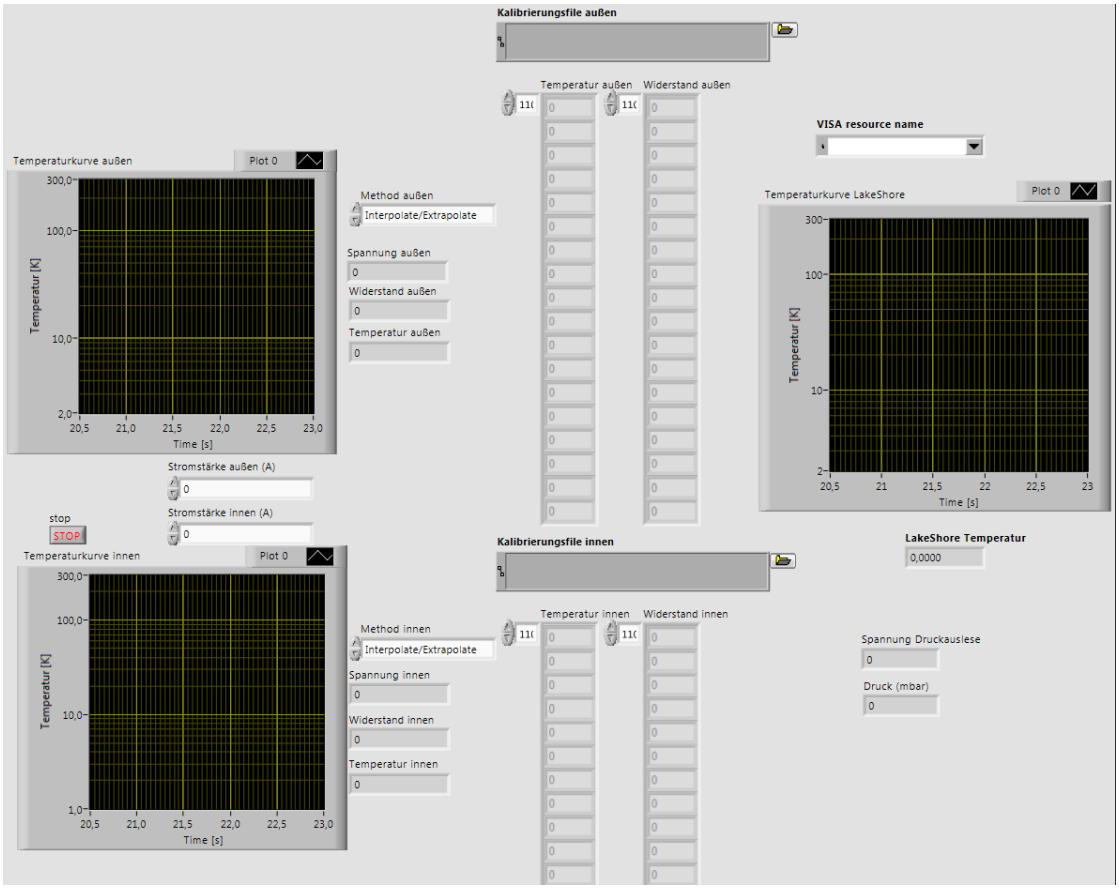

Figure 5.1.: Front Panel of the temperature readout LabView software. It can display the measurement of up to three different temperature sensors. Two sensors are controlled via the DAQ device whereas one sensor is controlled by a LakeShore Temperature Controller Model 331. Calibration files as well as the current for each DAQ controlled device must be entered by the user.

$0.38\,\mathrm{mm}^2$ connected the sensor with the electric circuit. A current of $I_1 = (96.1 \pm 0.3)\,\mu\mathrm{A}$ was applied by a static current generator. The current was measured by a MetraHit One multimeter and was double-checked with a Fluke 8846a high precision multimeter to verify that the first multimeter is able to measure currents on a μA scale. The cables were wired around the regenerator tubes of both stages to lower the temperature of the cable before it reaches the sensor. A small part of the cables was also attached firmly to the cold flanges of both stages by Kapton® tape. As mentioned above, a copper radiation shield was additionally applied to the second stage cold flange.
At the first stage cold flange, an additional TVO Tmi-CSS-D3-1337 temperature sensor was placed. It was connected in series to the sensor of the second stage. For the first measurement, it could only be monitored via a multimeter. However, later measurements also included it in the software which made it possible to save the data. The

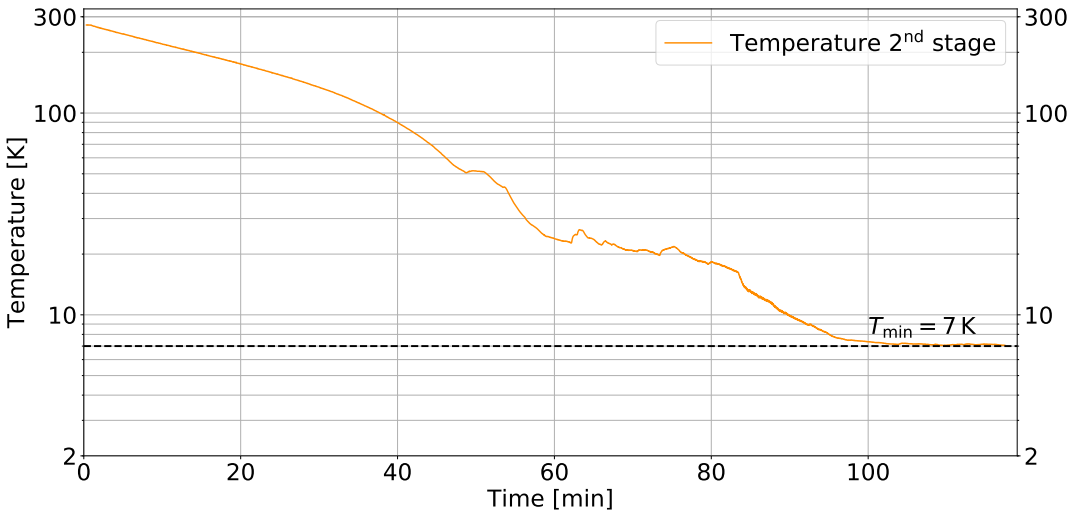

Figure 5.2.: First temperature measurement of the second stage cold flange. The curve shows significant artifacts below 60 K. The minimum temperature of 7 K is reached after 100 minutes.

same type of Teflon cables that was used for the sensor of the second stage was applied. These cables were wired around the regenerator tube of the first stage to ensure thermal coupling.
In the first 40 minutes the temperature curve shows the expected cooling behavior (compare fig. 3.7). A linear section in the beginning is followed by a steeper decline. The time until the final temperature is reached is also not significantly different. The second stage reached 100 K before 40 minutes have passed. After around 45 minutes, however, the curve starts to deviate from its original monotonically decreasing path. Between the 45^{th} and the 100^{th} minute artifacts can be noticed. In this section the temperature cure shows an unpredicted behavior although the temperature still decreases until it reaches its minimum of 7 K after 100 minutes which also does not match the expected temperature of under 4.2 K.
These issues needed to be addressed to prepare the coldhead for future experiments. At first the focus was laid on the compressor. Raising the helium pressure from 14 bar to around 17.5 bar improved the temperature curve by smoothing out the zig-zag behavior that was found below 60 K, although the minimum temperature remained unchanged.
Furthermore, thermal coupling of the wires that lead to the second stage was improved. This was done by guiding the wires over the top of the second stage cold flange with a batch of aluminum foil surrounding the cables. Additional kapton tapes further secured the wires at the regenerator tube. At the first stage, a firmly tightened small steel screw attached these cables to the cold flange.
Figure 5.3 shows the temperature curves of the second stage as well as the first stage after all the changes mentioned above have been implemented. One can see a big im-

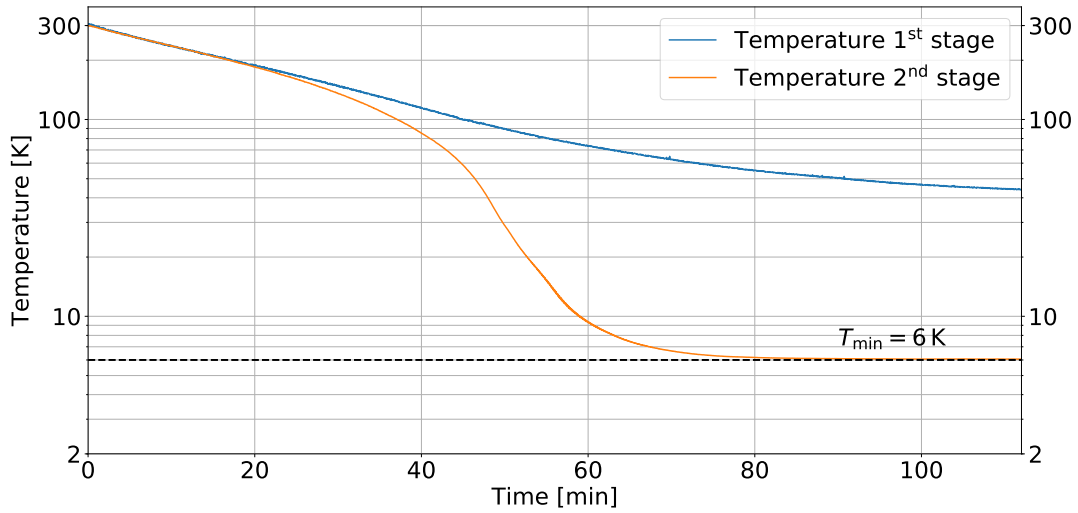

Figure 5.3.: Temperature curves of both cold flanges that were measured with an improved setup (compared to fig. 5.2). It featured a raised helium pressure of 17, 5 bar and improved thermal coupling of the wires leading to the sensors. The minimum temperature of the second stage (6 K) is reached after 80 minutes whereas the first stage reached a minimum temperature of 40 K after 150 minutes.

provement in comparison to the first measurement regarding the shape of the curve of the second stage. There are no artifacts below 60 K and the minimum temperature could be reduced to 6 K. Furthermore, the temperature curve of the first stage shows the expected behavior that can be seen in fig. 3.7. The minimum temperature of 40 K was reached after 150 minutes.
The calibration of the TVO sensors was done in 2007. This can lead to discrepancies between the measured temperature and the actual temperature. In order to be able to minimize uncertainties originating from the calibration a Cernox LakeShore CX-1050-SD temperature sensor was additionally installed to the second stage cold flange. The calibration for this device was done more recently in 2017. It was secured beneath a piece of indium and the block of copper which held the TVO sensor. The Cernox sensor was controlled by a LakeShore Temperature Controller Model 331 which was connected to the computer via USB so that the data could be collected by the LabView Software. The TVO sensor at the second stage was still mounted. However, its data is not used for analysis as it is only calibrated for temperatures higher than 3.623 K.
To finally reach the desired temperature value it was necessary to completely redo the wiring which included the replacement of the Teflon cables leading to the temperature sensors of the second stage with thinner AWG 34 wires (cross section: 0.02 mm^2). These were secured multiple times at the regenerator tube of the second stage and the first stage as well as at the cold flange of both stages (see fig. 5.4(a)) to ensure thermal

coupling over a large surface area. Aluminum foil was applied over the cables at the second stage cold flange to further increase thermal coupling. An additional protective layer of aluminum foil was applied over the entire cold flange as well as a big part of the regenerator and pulse tube (see fig. 5.4(b)). At last, the cables were wound around the outside of the copper radiation shield.

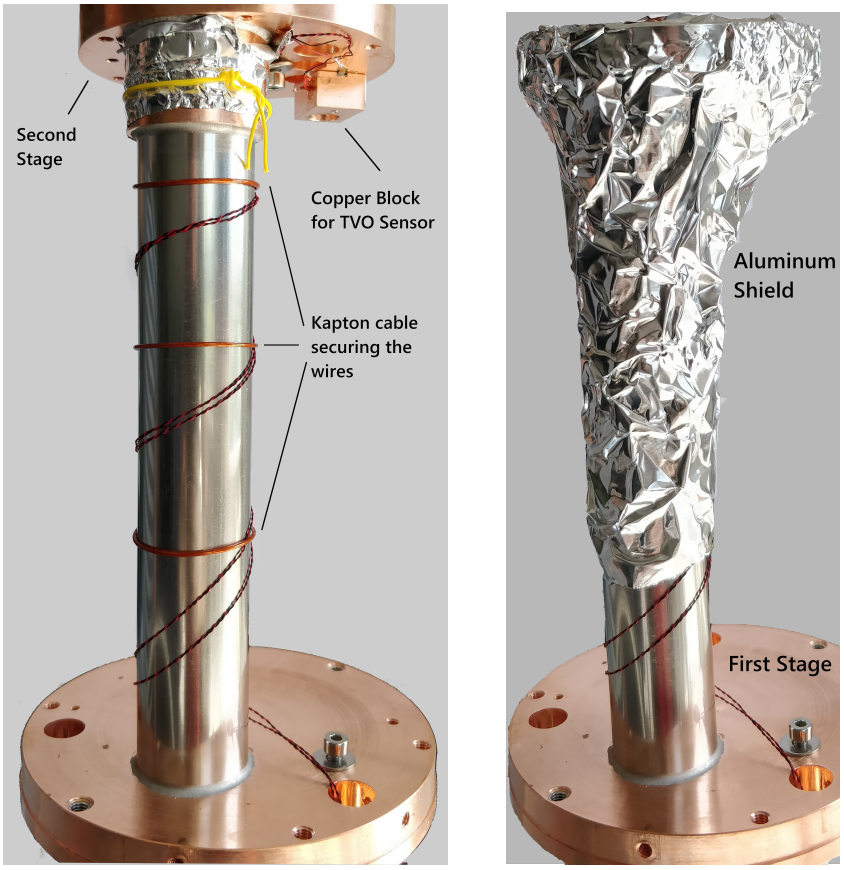

(a) (b)

Figure 5.4.: Final cabling of the wires leading to the temperature sensors at the second stage cold flange. (a) shows how the cables are attached to the regenerator tube and the cold flange. (b) shows the protective shielding made of aluminum foil. Not shown: Additional attachment of the wires to the copper radiation shield.

The temperature curves of both stages that were taken with this final setup are shown in fig. 5.5. During this measurement, the helium pressure inside the compressor was 16 bar. As can be seen, a minimum temperature of 2.5 K was measured at the second stage. The final temperature was reached after about 90 minutes. The first stage achieved a minimum temperature of 43 K after 200 minutes. Comparing this curve with the one TransMIT measured at their facilities (see fig. 3.7) there are only small differences in

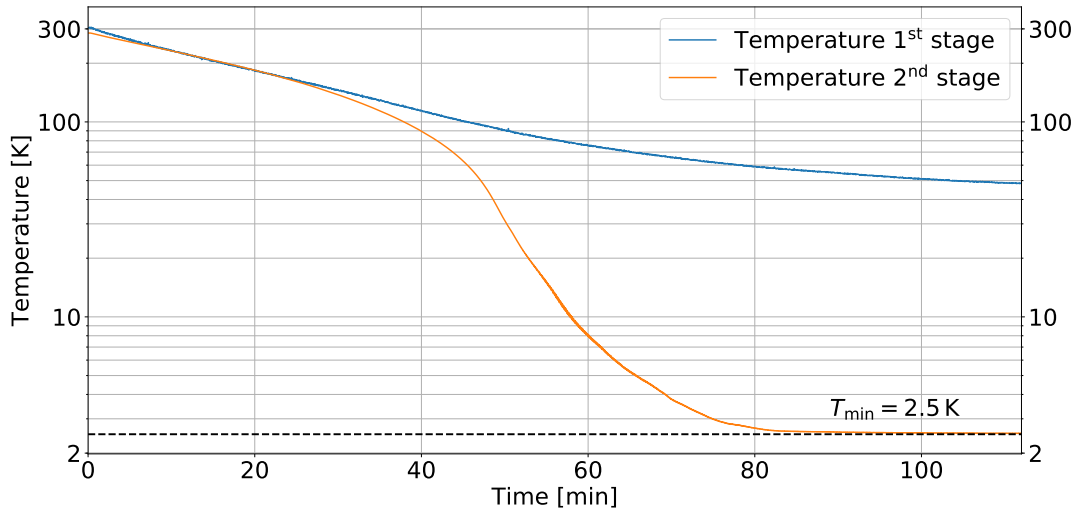

Figure 5.5.: Final temperature curves of both cold flanges. With all improvements the second stage reached a minimum temperature of 2.5 K after 90 minutes. The first stage reached a final temperature of 43 K after 200 minutes.

the shape of the curve. One noticeable effect is that the speed in which the temperature declines is slower than TransMIT measured. This becomes especially apparent when comparing the times after which 4.2 were achieved. In the example TransMIT provided 4.2 K were achieved after 54 minutes. In this case, however, it took 73 minutes which makes a difference of $\sim$ 35%. This deviation from the expected behavior is possibly caused by the usage of a different compressor but it needs to be monitored to assure that the cooling power of the coldhead is not affected.
A small calculation illustrates why correct wiring is important to achieve 2.5 K. Fourier's law of thermal conductivity in differential form is

$$\dot{Q} = \lambda(T) \cdot A \cdot \frac{\mathrm{d}T}{\mathrm{d}x} \tag{5.1}$$

where $\dot{Q}$ is the rate of heat flow, $\lambda(T)$ is the thermal conductivity of a material, $A = 0.02\,\mathrm{mm}^2$ is the cross sectional area and $\mathrm{d}T$ is the temperature difference between two points with a distance of $\mathrm{d}x$. As the thermal conductivity is not constant but temperature dependent, one needs to calculate the integral over the length of the wire

$$\dot{Q} = \frac{A}{l} \int_{T_L}^{T_H} \lambda(T)\,\mathrm{d}T \tag{5.2}$$

where T_H and T_L denote the respective temperature of the cable at the high temperature or low temperature side and l denotes the cable length. As the thermal conductivity curve of copper is strongly depends on its purity, this calculation is done using an

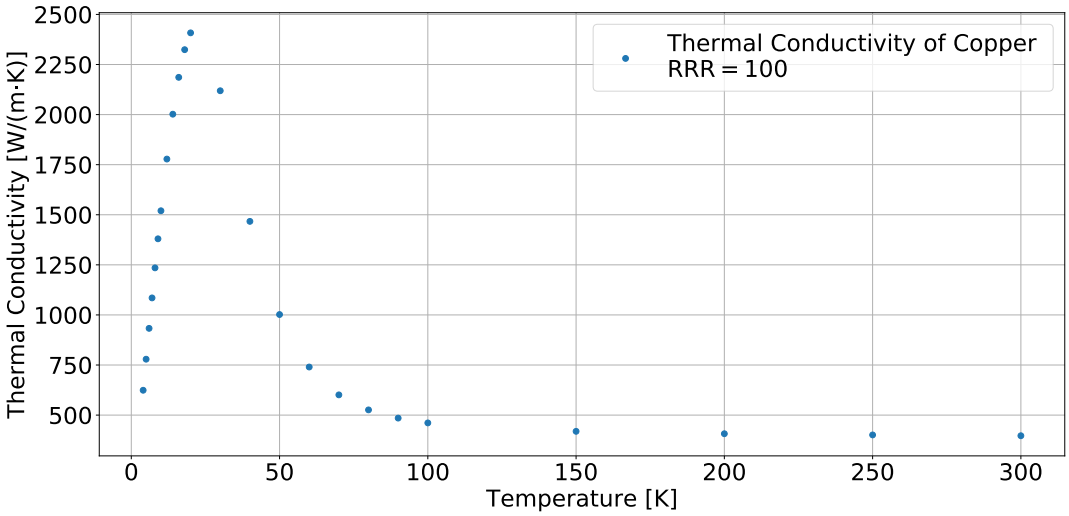

Figure 5.6.: Thermal Conductivity of Copper with a RRR value of 100. Values are taken from [29].

exemplary heat conductivity curve of copper with a residual resistance value (RRR; ratio of electrical resistivity at 4.2 K to the electrical resistivity at 273 K) of 100. This curve is shown in fig. 5.6.
Calculating the integral from eq. (5.2) with $T_L = 4\,\mathrm{K}$, $T_H = 300\,\mathrm{K}$ and $l = 0.5\,\mathrm{m}$ yields a heat flow of 8.7 mW. This represents the case where the wire is not sufficiently connected to a cold point of the refrigerator. If this is the case, however, then $T_H = 40\,\mathrm{K}$ and the heat flow is 2.8 mW which is a significant improvement by a factor 3.
Even more important, however, is the proper attachment of the wires to the second stage cold flange. cryo.TransMIT specifies the cooling power of the second stage with 0.95 W at 4.2 K. As for the thermal conductance $\dot{Q} \ll 0.95\,\mathrm{W}$ holds the wires can easily be cooled down $< 4\,\mathrm{K}$ by the second stage. If the wires maintain the temperature of the second stage until reaching the sensor, there is no thermal conduction at all. Only the electrical power

$$P = U \cdot I = R \cdot I^2 \tag{5.3}$$

will then influence the temperature measurement. For resistance $R \approx 3000\,\Omega$ and current $I \approx 40\,\mu\mathrm{A}$) the electrical power is estimated to be in the region of $1 - 20\,\mu\mathrm{W}$, which means that the influence of electrical power on the temperature measurement can be neglected.

With these measurements it can be confirmed that the PTD 406C pulse tube cooler works and is applicable in the TOF setup. It can also be concluded that in a cryogenic environment with temperatures below 10 K it is immensely important to minimize external heat sources. Renewing the cabling in a way that both cold flanges as well as

both regenerator tubes and the surrounding copper shield served as cold points to lower the cables' temperature before reaching the temperature sensor had a significant impact to reach a minimum of 2.5 K at the second stage cold flange. It is also recommended to regularly check the helium pressure inside the compressor to avoid artifacts in the temperature curve.

6. Conclusion and Outlook

In this thesis a new setup to investigate time-of-flight techniques is presented. Electrons emitted from an angular-selective UV photoelectron source propagate through two beam tubes that use the MAC-E filter principle. In the middle of the setup the installation of a 4 K cryocooler is intended to examine possible solutions for an electron tagger device. The general functionality of the electron source was tested at a backplate voltage of $U_{\text{back}} = -13\,\text{kV}$ and the successful emission of electrons was verified. To obtain a spectrum with gaussian peaks it is recommended to generate electrons with kinetic energies larger than 15 keV. Nevertheless, 13 keV electrons can be used to understand the fundamental properties of the system. Furthermore, this condition only applies for the SI-PIN detector which will be replaced by a MCP in the final setup.
Several simulations were conducted to homogenize the magnetic field and to investigate the adiabaticity as well as the transmission properties of the new TOF setup. It was found that there is a noticeable difference between the magnetic moments inside the first and second electrode which has impacts on the time-of-flight, the angle θ as well as the kinetic energy components $E_{\parallel}$ and $E_{\perp}$. With the simulation data one can adjust the setup configuration with respect to the sensitivity requirements of the measurement. For example, the impact on the time-of-flight can be minimized by using start angles $\theta_{\text{start}} \ll \theta_{\text{max}}$ where θ_{max} is the maximum transmission angle of the respective configuration. Furthermore, adiabaticity violations can occur within the electrode regions. This is correlated to the surplus energy and the current I_c. Lower currents require smaller surplus energies to avoid these effects.
The investigation of the transmission properties further revealed several limiting factors. Due to the setup of the electrode the electric potential slows down electrons before the corresponding momenta are collimated. This leads to the effect of early retardation which reduces the maximum transmission angle at given surplus energies. One method to minimize the influence of this effect includes an additional coil that is located between the electrode and the first main coil. By applying an electric current in the opposite direction the magnetic field could be shaped in a way that the electron momenta are mostly collimated before they enter the electrode.
Another method proposes the usage of a segmented electrode where each segmentation can be set to a different retarding potential. This would change the shape of the electric field in such a way that the maximum retarding potential is reached at a later point in the spectrometer. This allows the momenta of the electrons to be collimated before being significantly affected by the retarding potential. Both methods can also be used simultaneously to optimize the electromagnetic field configuration.
A helium based two-stage 4 K pulse tube cooler has been tested and its cooling capabilities could be verified so that electron tagger devices can be tested in the future. A

temperature of 2.5 K was measured at the second stage cold flange. Measurement of this temperature requires correct wiring. The wires leading to the temperature sensor need to be sufficiently thermally coupled in order to minimize thermal conduction from the wires to the temperature sensor.
After the commissioning of the TOF setup, first measurements will be performed to verify the simulation results. While the adiabaticity and transmission properties of the setup were calculated within this thesis, further simulations are required in order to perform TOF experiments.

A. Appendix

Electron Spectrum

Background Modeling (Lognormal Distribution):

$$f(x) = \frac{A}{\sqrt{2\pi}\sigma(x-c)} \exp\left(-\frac{(\ln(x-c)-\mu)^2}{2\sigma^2}\right) + d,\ x-c>0 \tag{A.1}$$

Table A.1.: Values of the background fit in fig. 3.5

A	432 ± 3
σ	0.47 ± 0.01
μ	2.63 ± 0.02
c	106.3 ± 0.3
d	3.8 ± 0.3

Fit of the electron spectrum:

$$g(x) = \sum_{i=1}^{3} \frac{A_i}{\sqrt{2\pi\sigma_i^2}} \exp\left(-\frac{(x-\mu_i)^2}{2\sigma_i^2}\right) \tag{A.2}$$

Table A.2.: Values of the fit for the electron spectrum in fig. 3.5

A_1	2665 ± 729
σ_1	6.6 ± 0.3
μ_1	124.4 ± 0.3
A_2	2330 ± 785
σ_2	9.7 ± 1.4
μ_2	135.4 ± 2.9
A_3	959 ± 71
σ_3	15.8 ± 1.1
μ_3	170.7 ± 1.3

TOF Setup

(a)

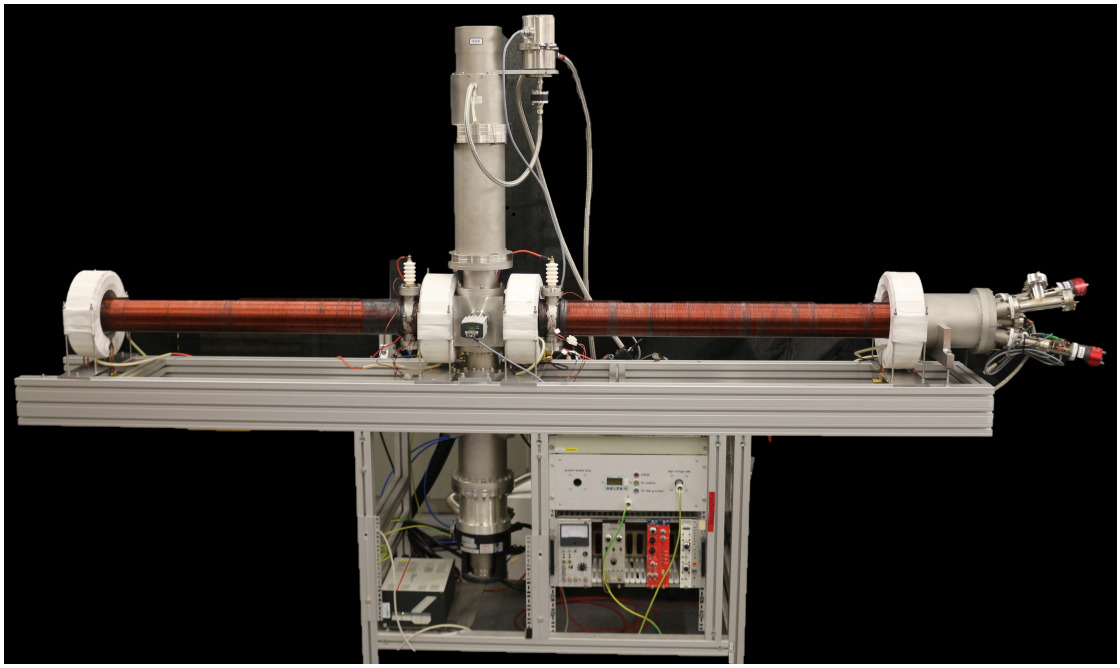

(b)

Figure A.1.: Partly finished TOF setup with the 4 K coldhead installed. Pictures by K. Gauda (personal communication, October 2019).

Bibliography

[1] V. N. Aseev et al. "Upper limit on the electron antineutrino mass from the Troitsk experiment". In: *Physical Review D* 84.11 (Dec. 2011). ISSN: 1550-2368. DOI: 10.1103/physrevd.84.112003. URL: http://dx.doi.org/10.1103/PhysRevD.84.112003.

[2] Ch Kraus et al. "Final results from phase II of the Mainz neutrino mass search in tritium beta-decay". In: *The European Physical Journal C-Particles and Fields* 40.4 (2005), pp. 447–468.

[3] KATRIN collaboration. *KATRIN design report 2004*. 2005.

[4] M Aker et al. "An improved upper limit on the neutrino mass from a direct kinematic method by KATRIN". In: *arXiv preprint arXiv:1909.06048* (2019).

[5] Y. Fukuda et al. "Evidence for Oscillation of Atmospheric Neutrinos". In: *Physical Review Letters* 81.8 (Aug. 1998), 1562–1567. ISSN: 1079-7114. DOI: 10.1103/physrevlett.81.1562. URL: http://dx.doi.org/10.1103/PhysRevLett.81.1562.

[6] *Windowless Gaseous Tritium Source (WGTS). Where the beta electrons start their journey*. Karlsruhe Institute of Technology. Sept. 12, 2019. URL: http://www.katrin.kit.edu/766.php.

[7] Oliver Rest. "Precision high voltage at the KATRIN experiment and new methods for an absolute calibration at ppm-level for high-voltage dividers". In: (2019-07).

[8] Nicholas Steinbrink et al. "Neutrino mass sensitivity by MAC-E-Filter based time-of-flight spectroscopy with the example of KATRIN". In: *New Journal of Physics* 15.11 (2013), p. 113020.

[9] Alexander Fulst. *Investigations of Time-of-Flight Methods for the KATRIN Experiment*. Master Thesis. Aug. 26, 2016.

[10] G Beamson, H Q Porter, and D W Turner. "The collimating and magnifying properties of a superconducting field photoelectron spectrometer". In: *Journal of Physics E: Scientific Instruments* 13.1 (Jan. 1980), pp. 64–66. DOI: 10.1088/0022-3735/13/1/018. URL: https://doi.org/10.1088%2F0022-3735%2F13%2F1%2F018.

[11] Karen Hugenberg. *Design of the electrode system for the KATRIN main spectrometer*. Diploma Thesis. 2008.

[12] Jan Behrens. “Design and Commissioning of a Monoenergetic Photoelectron Source and Active Background Reduction by Magnetic Pulse at the KATRIN Experiment”. PhD thesis. Institut für Kernphysik - Westfälische Wilhelms-Universität Münster, 2017.

[13] JD Jackson. *Classical Electrodynamics*. pp. 419–424. John Wiley & Sons Ltd., 1962.

[14] Nicholas Steinbrink. “Simulation of Electron Neutrino Mass Measurements by Time-of-Flight with KATRIN”. Diploma Thesis. Institut für Kernphysik - Westfälische Wilhelms-Universität Münster, May 2012.

[15] J Behrens et al. “A pulsed, mono-energetic and angular-selective UV photo-electron source for the commissioning of the KATRIN experiment”. In: *The European Physical Journal C* 77.6 (2017), p. 410.

[16] Michael Zacher. “High Field Electrodes Design and an Angular Selective Photoelectron Source for the KATRIN Spectrometers”. PhD thesis. Institut für Kernphysik - Westfälische Wilhelms-Universität Münster, 2015.

[17] tectra GmbH, ed. *MCP Assembly*. July 2017.

[18] tectra GmbH, ed. *Microchannel Plate – Nude*. July 2017.

[19] Benedikt Bieringer. *MCA Recorder*. 2019. URL: `https://nuserv.uni-muenster.de:8443/wwu-git/mca-recorder/tree/master/`.

[20] Eric W. Weisstein. *Log Normal Distribution*. From MathWorld–A Wolfram Web Resource. Sept. 12, 2019. URL: `mathworld.wolfram.com/LogNormalDistribution.html`.

[21] Jens Falter. *Pulse Tube Cryocooler. Solutions for Customized Dry Low-Noise-Cryostats*. Oct. 28, 2019.

[22] William E Gifford and RC Longsworth. “Pulse-tube refrigeration”. In: *Journal of Engineering for Industry* 86.3 (1964), pp. 264–268.

[23] Alphons De Waele. “Pulse-tube refrigerators: principle, recent developments, and prospects”. In: *Physica B: Condensed Matter* 280 (May 2000), pp. 479–482. DOI: `10.1016/S0921-4526(99)01840-2`.

[24] Ray Radebaugh. “Development of the Pulse Tube Refrigerator as an Efficient and Reliable Cryocooler”. In: *Proceedings of the Institute of Refrigeration* 96 (Jan. 2000).

[25] TransMIT-Center for Adaptive Cryotechnology and Sensors. *Two-Stage 4 K Pulse Tube Cooler PTD 406C UHV (SN 082). User Manual*. Apr. 2019.

[26] Ferenc Glück et al. *BField_3D - Magnetic field calculation for cylincdrical coils*. 2019. URL: `https://nuserv.uni-muenster.de:8443/bbieringer/bfield_3d`.

[27] Daniel Furse et al. “Kassiopeia: a modern, extensible C++ particle tracking package”. In: *New Journal of Physics* 19.5 (2017), p. 053012.

[28] Ferenc Glück. “Axisymmetric magnetic field calculation with zonal harmonic expansion”. In: *Progress In Electromagnetics Research* 32 (2011), pp. 351–388.

[29] N. Simon, Elizabeth Drexler, and R. Reed. “Properties of Copper and Copper Alloys at Cryogenic Temperatures”. In: *NIST Monograph* 177 (Jan. 1992).